



HAL
open science

Timing, volume and precursory indicators of rock- and cliff fall on a permafrost mountain ridge (Mattertal, Switzerland)

Hanne Hendrickx, Gaëlle Le Roy, Agnès Helmstetter, Eric Pointner, Eric Larose, Luc Braillard, Jan Nyssen, Reynald Delaloye, Amaury Frankl

► To cite this version:

Hanne Hendrickx, Gaëlle Le Roy, Agnès Helmstetter, Eric Pointner, Eric Larose, et al.. Timing, volume and precursory indicators of rock- and cliff fall on a permafrost mountain ridge (Mattertal, Switzerland). *Earth Surface Processes and Landforms*, 2022, 57 (6), pp.1532-1549. 10.1002/esp.5333 . hal-03603637

HAL Id: hal-03603637

<https://hal.inrae.fr/hal-03603637>

Submitted on 14 Oct 2022

HAL is a multi-disciplinary open access archive for the deposit and dissemination of scientific research documents, whether they are published or not. The documents may come from teaching and research institutions in France or abroad, or from public or private research centers.

L'archive ouverte pluridisciplinaire **HAL**, est destinée au dépôt et à la diffusion de documents scientifiques de niveau recherche, publiés ou non, émanant des établissements d'enseignement et de recherche français ou étrangers, des laboratoires publics ou privés.

1 **Integration of high resolution records for understanding the processes behind a disintegrating**
2 **permafrost rock face, Mattertal, Switzerland.**

3
4 **Abstract:** Rockfall sites often represent a challenging study object due to a complex interaction
5 between site-specific conditions such as geology, topography and meteorology on the one hand and
6 their inaccessibility on the other hand. Therefore, the combination of several close-range remote
7 sensing techniques were used to offer a detailed account of 339 rock- and cliff fall events ($< 10 - 31$
8 300 m^3) observed in a timespan of four years (2017-2020) at a south facing rock face at Grosse Grabe
9 in Mattertal (Western Swiss Alps), depositing more than $200\,000 \text{ m}^3$ of debris. Large cliff falls (10^4 - 10^6
10 m^3) were precluded by an outward movement that started to increase 1.5 years before any significant
11 collapse of the rock face and reaching locally up to 30 cm. This progressive displacement of the rock
12 face was more pronounced in summer, indicating thermal induced failure mechanism were at play at
13 fracture level. In addition, ice cementation in the clefts could have played a stabilising role in the
14 winter. The largest cliff fall events occurred in summer and systematically exposed ice in the clefts.
15 This is assumed to be the base of the permafrost from the north side, because the collapsing south
16 face is unsuitable for permafrost to occur. The presented dataset is unique because data collection
17 started before the onset of the rock wall destabilisation and collapse, allowing to get insight into the
18 processes at play prior to large rock- and cliff fall. Highly fractured south-exposed gneiss lithology is
19 viewed as the main precondition for the observed rockfall events, allowing high temperature
20 oscillations to cause irreversible movements at fracture level. Rapid permafrost degradation is viewed
21 as a triggering factor after its exposure, causing progressive failure of the rock wall leading to very high
22 rock wall erosion rates on a decadal timescale.

23
24 **Keywords:** Terrestrial laser scanner, photogrammetry, rockfall, seismology, mountain permafrost,
25 structural predisposition

26 **1. Introduction**

27 Rockfall, i.e. the downward free or bounding movement of rock detachments from steep
28 rock walls, is a common geomorphic phenomenon in steep relief (Luckman, 2013) and an
29 important rockwall erosion agent (Krautblatter and Moore, 2014). Rockfall usually describes
30 detachments of a magnitude up to 10^4 m^3 (Dussauge, Grasso and Helmstetter, 2003), ranging
31 from boulder falls (10^1 - 10^2 m^3), debris falls ($< 10^3 \text{ m}^3$) and block falls (10^2 - 10^4 m^3) (Krautblatter,
32 Funk and Günzel, 2013). Larger magnitude events are defined as cliff falls (10^4 - 10^6 m^3), rockslides
33 and rock avalanches ($>10^6 \text{ m}^3$) (Krautblatter, Funk and Günzel, 2013). Geological structures and

34 related fracture geometry and density are important predisposition factors for rock wall
35 instability leading to rockfall (Gunzburger, Merrien-Soukatchoff and Guglielmi, 2005; Hasler,
36 Gruber and Beutel, 2012; Beniston *et al.*, 2018). Temperature oscillations, both on daily, seasonal
37 and annual timescales, can serve as a potential preparatory factor. The expansion and contraction
38 of rock can cause thermal stress fatigue and small irreversible displacements of rock fractures
39 (Gunzburger, Merrien-Soukatchoff and Guglielmi, 2005; Collins and Stock, 2016; Weber *et al.*,
40 2017; Bakun-Mazor *et al.*, 2020). When seasonal or permanent ice is present in the rock wall,
41 temperature cycles drive cryogenic processes such as ice segregation and volumetric expansion
42 (Matsuoka, 2008), leading to rockwall erosion by frost weathering (Krautblatter and Dikau, 2007;
43 Draebing and Krautblatter, 2019). Rockfall is therefore particularly common in the high mountain
44 environment experiencing seasonal frost or permafrost (Fischer *et al.*, 2012; Ravanel, Magnin and
45 Deline, 2017). In periglacial areas, rockfall events mostly occur in the warm half of the year (Sass,
46 2005c), triggered for example by rainfall (Helmstetter and Garambois, 2010; Dietze, Turowski, *et*
47 *al.*, 2017), diurnal temperature changes (Dietze, Turowski, *et al.*, 2017) and freeze-thaw
48 transitions (Luckman, 2013; Dietze, Turowski, *et al.*, 2017). Because of this, rockfall activity is
49 often higher during spring and autumn (Gardner, 1983; Luckman, 2013; Dietze, Turowski, *et al.*,
50 2017). North-facing rockwalls also experience more frost action due their high moisture levels
51 and lower average temperatures, leading to enhanced rockfall activity (Gardner, 1983; Sass,
52 2005b). This highlights that climatic factors are crucial for rock wall stability as well, since they
53 control weathering processes (Sass, 2005a; Draebing and Krautblatter, 2019) and affect bedrock
54 permafrost, the latter possibly subjected to fast change (Gruber and Haeberli, 2007). In this
55 context, climate change can modify the rockfall susceptibility and the related hazard risk
56 (Haeberli and Beniston, 1998). Warming permafrost and increasing seasonal thaw depth can alter
57 the stability of steep rock faces (Noetzli *et al.*, 2007; Fischer *et al.*, 2012; Draebing, Krautblatter
58 and Dikau, 2014) by the failure of ice-filled rock fractures due the lowering of shear resistance
59 with increasing temperature (Davies, Hamza and Harris, 2001). Areas characterized by warm
60 permafrost (between -2°C and 0°C) will first be affected by this process. For mountains flanked
61 by densely populated areas, like the European Alps, rockfall is particularly hazardous, affecting
62 communities, infrastructures and economies at lower elevations (Gruber and Haeberli, 2007;
63 Walter *et al.*, 2019).

64 In the last three decades, an increase rockfall events ($< 10^4 \text{ m}^3$) have been observed in
65 permafrost areas in many places of the European Alps, often related to summer heatwaves that
66 cause excessive permafrost thawing from the surface, deepening the active layer (Gruber, 2004;
67 Fischer *et al.*, 2011; Stoffel and Huggel, 2012; Ravanel, Magnin and Deline, 2017). An increase in
68 larger rockfall or cliff fall events (10^4 - 10^6 m^3) has been observed as well (Fischer *et al.*, 2012),

69 caused by failure at greater depth as the consequence of a gradual permafrost degradation,
70 rather than active layer thaw (Gruber and Haeberli, 2007; Allen and Huggel, 2013). Very large
71 rock slope failures, often referred to as rockslides or rock avalanches ($> 10^6 \text{ m}^3$), can occur at any
72 time of the year (Phillips *et al.*, 2017) and are not necessarily linked to areas where warm
73 permafrost occurs (Hasler *et al.*, 2011). In these cases, the rockfall occurrence is primarily
74 controlled by the lithological settings of the site (Fischer *et al.*, 2012) and by the slow change in
75 fracture toughness of rock bridges due to warming (Krautblatter, Funk and Günzel, 2013).
76 Unprecedented large scale cliff falls, rockslides and rock avalanches may substantially affect the
77 alpine sediment cascade, providing fragmented rock debris on talus slopes, glaciers, rock glaciers
78 and in high alpine torrents. Such unconsolidated sediments may for instance be remobilized by
79 rainfall-triggered debris flows and cause infrastructural damage to downstream communities
80 long after the initial rockfall event (Baer *et al.*, 2017).

81

82 To increase the understanding of rock wall instability and its development, important for
83 predicting process dynamics and mitigating hazards (McColl and Draebing, 2019), related rockfall
84 frequencies and magnitudes need to be monitored (Fischer *et al.*, 2012). Terrestrial laser scanning
85 (TLS) and Uncrewed Aerial Vehicle (UAV) data can provide accurate 3D-information about rock
86 face geometry, allowing to derive rockfall location and volume when repeated measurements are
87 done. Precursory indicators before failure such as cleft opening or pre-failure deformation of a
88 few cm can also be detected if the accuracy of the method allows it (Abellán *et al.*, 2010).
89 However, multiple rockfall releases within one monitoring period cannot be resolved using
90 TLS/UAV data (Dietze, Mohadjer, *et al.*, 2017). Automatic camera images can help identify
91 different events, but only when visibility allows it (and thus e.g. not during the night or foggy
92 conditions). Rockfall events can also be studied by analysing the characteristic seismic pulses they
93 cause. In contrast to TLS/UAV data, seismic data does not rely on survey intervals (Dietze,
94 Mohadjer, *et al.*, 2017; Le Roy *et al.*, 2019) or visibility conditions (Dietze, Mohadjer, *et al.*, 2017).
95 Seismic data can therefore be used for real-time detection and warning. Moreover, the link
96 between external factors influencing the rockfall event can be studied better if the exact timing
97 of the latter is known (Dietze, Mohadjer, *et al.*, 2017; Le Roy *et al.*, 2019). Relationships between
98 rockfall event properties (detachment and impact areas, volume, geometry and propagation) and
99 the seismic signal can also be applied in different geological settings and for different rockfall
100 magnitudes (Le Roy *et al.*, 2019). Combining different datasets is therefore essential for rockfall
101 characterisation (Fischer *et al.*, 2011; Dietze, Mohadjer, *et al.*, 2017). Although it is rare to have
102 data from initial destabilisation up to failure of a rock face, this information is of high importance
103 for adopting early warning systems (Leinauer, Jacobs and Krautblatter, 2020).

104 The main aim of this study is to accurately present the temporal and spatial distribution
 105 of all rockfall events that occurred at a disintegrating south-facing rock face (2600 – 2700 m a.s.l.)
 106 in Mattertal, Switzerland. To achieve this, a combination and integration of four different
 107 datasets (UAV, TLS, seismic and automatic camera data) were used. By doing so, this study
 108 provides valuable information for rockfall hazard management and contributes toward the
 109 understanding of the processes involved in large rock- and cliff fall, having increasingly occurred
 110 in high mountain environments during the last three decades (Huggel *et al.*, 2012). While post-
 111 event remote sensing is common to study rockfall in the periglacial high mountain environment
 112 (Fischer *et al.*, 2011; Dietze, Mohadjer, *et al.*, 2017; Le Roy *et al.*, 2019; Sala, Hutchinson and
 113 Harrap, 2019), it is rare to have direct observations before, during, and after rockfall. Here, we
 114 present such a unique dataset (2017 – 2020), resulting in valuable information about precursory
 115 processes, temporal distribution and potential triggers of rockfall. This study benefited greatly
 116 from the datasets available from seismic and automatic camera installations, already in place for
 117 rock glacier monitoring and their relationship to debris flow activity (Kummert, Delaloye and
 118 Braillard, 2018; Guillemot *et al.*, 2020).
 119

120 **2. Study site, material and methods**

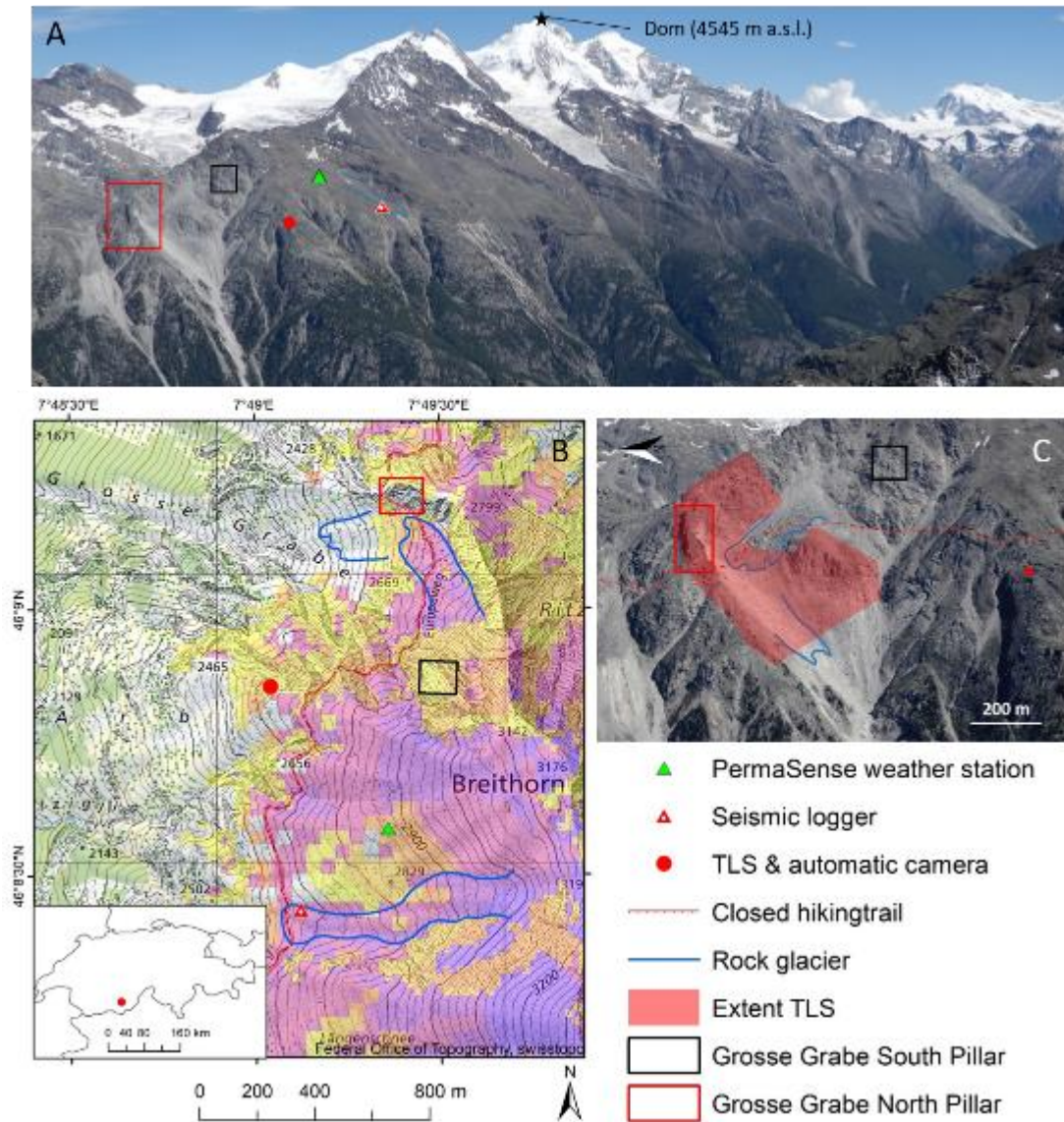
121 **Table 1.:** Overview of application and integration of the various methods used in this study

	Fixed installations for the monitoring of rock glaciers			
	TLS	UAV	Seismics	Time-lapse camera
Start of the monitoring	2017	2020	2015	2011
Temporal resolution	Bi-annual (10 scans)	Weekly (5 surveys)	Continuous	Hourly
Spatial accuracy	3 cm	30 cm	Low, only one logger	High qualitative confirmation of rockfall
Spatial extent	Grosse Grabe North Pillar and adjacent rock wall	Grosse Grabe North Pillar	Grosse Grabe North Pillar, South pillar and environments	Grosse Grabe North Pillar
Remarks	<ul style="list-style-type: none"> • Topographic occlusion due to single scan position • Cumulative volumes • Precursory deformation 	<ul style="list-style-type: none"> • No topographic occlusion • Visual information • Event based volumes 	<ul style="list-style-type: none"> • All rockfall recorded • Estimated volumes • No exact rockfall location 	<ul style="list-style-type: none"> • Near real-time confirmation of rockfall and location • Precursory fracture widening • Qualitative data

122 TLS: terrestrial laser scanning, UAV: uncrewed aerial vehicle

123

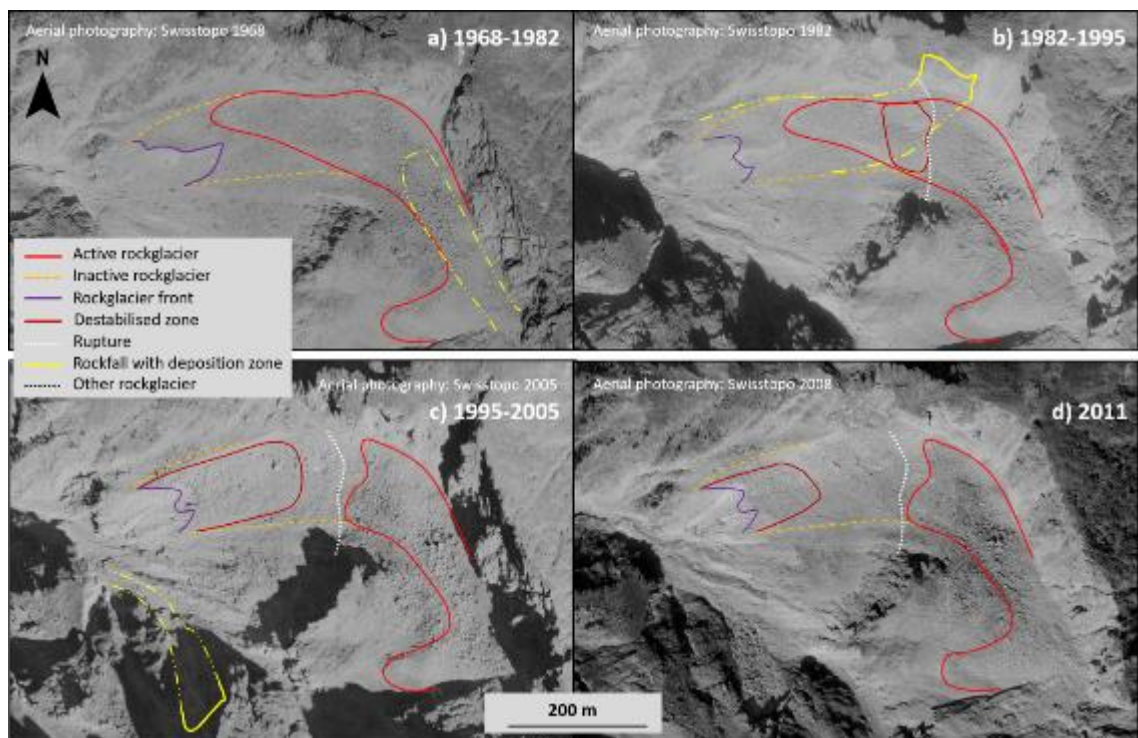
124 **2.1. Study area**



125
 126 **Figure 1.:** The study area: a) The environment of the rock face studied and the monitoring
 127 installations in place for the study of nearby rock glaciers, together with the position of the
 128 laserscan, which was specifically executed for the monitoring of Grosse Grabe North Pillar. The
 129 Dom is the highest summit of the area at 4545 m a.s.l. and the treeline is located at about 2300
 130 m a.s.l., b) Potential permafrost distribution in the environment displayed on the topographic
 131 map (SwissTopo), ranging from yellow for patchy permafrost in favourable conditions and dark
 132 purple/blue for extensive permafrost in nearly all conditions (Boeckli *et al.*, 2012), c) insert of the
 133 study area, displaying the extent of the terrestrial laser scans.

134
 135 The study area is an unstable south-facing rock face (2600 – 2700 m a.s.l.), North of the
 136 Grosse Grabe torrent (and hereafter referred to as Grosse Grabe North Pillar) and its adjacent
 137 rock wall, at the orographic right side of the Matternal valley, Switzerland (46°09'08"N, 7°49'21"E,
 138 Figure 1). The lithological structure consists of highly fractured augen gneiss with a foliation dipping

139 SW, interlaced with various tectonic cleft structures (Bearth, 1978). The studied rock face is part
 140 of a narrow ridge with a height of 100 – 120 m. The first monitored rock fall activity at Grosse
 141 Grabe North Pillar occurred in the mid-1980s, as observed in historical aerial photographs (Figure
 142 2b, Delaloye *et al.*, 2014). The rock glacier at the base of the rock face was overburdened by these
 143 deposits and reaccelerated rapidly (velocities up to 5 m per year between 1995 and 2010). Because of
 144 this, the upper and currently intact part of the rock glacier, not impacted by the rockfall of the 1980s,
 145 is separated from the lower terminal tongue (Figure 2c-d, Delaloye *et al.*, 2013). The movement of the
 146 terminal tongue has been decreasing since 2010 (Delaloye *et al.*, 2013) and had become very slow
 147 when the survey of the lower section stopped in 2017 (< 0.5 m/yr). This marks the end of the
 148 destabilisation phase of the rock glacier, likely indicating the almost completed permafrost
 149 degradation at depth, in analogy to the attested absence of permafrost in the well-developed rupture
 150 zone of a similarly destabilised rock glacier (Delaloye and Morard, 2011). Rock wall instabilities in the
 151 surroundings of the study area are common as well, with isolated rockfall from the same ridge in the
 152 1970s (Figure 2a, Delaloye *et al.*, 2014). More recent rockfall from an area more to the south of the
 153 studied rock face (Grosse Grabe South Pillar, Figure 1) led to the closure of the hiking trail crossing
 154 the area in 2018.



155
 156 **Figure 2.** Orthophotos revealing the historical development of the site related to rockfall activity,
 157 a) isolated rockfall from the same ridge occurring in the 1970s, b) rockfall from Grosse Grabe
 158 North Pillar occurring in the mid-1980s, overburdening the rock glacier below, c) and d) the
 159 development of the rupture of the rock glacier.

160

161 The studied rock face is below the lower limit of permafrost occurrence of south faces, which
162 is around 3300 m a.s.l. in the Mont Blanc Massif (Magnin *et al.*, 2017) and around 2900 m a.s.l. in the
163 Swiss Alps, for ice-poor permafrost (Kenner, Noetzli, *et al.*, 2019). However, permafrost may exist in
164 the studied rock wall because of the opposite north face, here in a distance of approx. 50 – 70 m
165 across the pillar. Indeed, the potential permafrost distribution map shows that local permafrost likely
166 to be found at the north face and absent at the south face of Grosse Grabe (Figure 1, Boeckli *et al.*,
167 2012). Moreover, the highly fractured bedrock favours bedrock cooling by the convection of cold air
168 (Moore *et al.*, 2011) and the trapping of snow in winter time (Hasler, Gruber and Haeberli, 2011). All
169 of the above makes permafrost presence in the studied rock wall likely.

170

171 2.2. Meteorological data

172 A long term record of high temporal resolution meteorological data is available from Grächen
173 station (MeteoSwiss, 46°11'42"N, 7°50'09"E at 1605 m a.s.l., approx. 5 km from the study area, same
174 orographic side of the valley); this meteorological station has measured air temperature and
175 precipitation since 1864, with automatically measured data available since 2013. Annual mean
176 precipitation at this station is 625 ± 120 mm for the reference period of 1981 – 2010. There is low
177 seasonality in precipitation, with October the wettest month (63 ± 52 mm), and January through April
178 the driest months (30–40 mm on average) (Stoffel, Tiranti and Huggel, 2014, MeteoSwiss). Mean
179 annual air temperature (MAAT) at the meteorological station is around 5.3 ± 0.7 °C (1981-2000)
180 (MeteoSwiss). A shorter temperature record (2012-2020) with a 2-minute interval is available
181 from a weather station located on the Breithorn landslide (2873 m a.s.l.), 1 km from the study
182 area (Figure 1), revealing a MAAT of -0.3 ± 0.7 °C. This weather station is deployed by PermaSense,
183 a consortium of researchers and research projects developing and operating autonomous sensing
184 systems in high-mountain environments for acquiring long-term datasets (*UZH - The PermaSense*
185 *Consortium*, 2021). Temperature data of the PermaSense station correlates well linearly with the
186 temperature record of Grächen ($R^2 = 0.97$), corresponding to a lapse rate of 4.9 ± 1.03 C° km⁻¹.
187 This linear relationship justifies the use of the Grächen temperature record when data gaps occur
188 in the PermaSense station. Within this study, temperature and precipitation data is used to detect
189 relationships between rockfall and frost/thaw and wet/dry cycles, as shown by other studies
190 (Helmstetter and Garambois, 2010; Bajni, Camera and Apuani, 2020). To do this, the cross-correlation
191 function was established between temperature or precipitation data from the more complete Grächen
192 series and the rate of rockfalls detected from the seismic network. This highlights the potential

193 triggering effect of precipitation/temperature without defining a threshold and provides the time
194 delay between a certain meteorological event and the occurring rockfall. For a detailed description of
195 the methodology, see Helmstetter and Garambois (2010). Local temperature data from the
196 PermaSense station was used to detect if any specific event precluded the largest rock – and cliff
197 fall observed ($> 5000 \text{ m}^3$), using a simple t-test comparing weekly temperature averages on the
198 95% significance level.
199

200 *2.3. Hourly terrestrial time-lapse photography*

201 Monitoring of rockfall occurrence can be achieved by photographic surveys using fixed
202 installations (D'Amato *et al.*, 2016; Matsuoka, 2019). In this study, the observation of the rock face
203 started in 2011 with the hourly archival of images taken by an automatic camera (Table 1, Figure 3).
204 The latter was installed to study the rock glaciers underneath the face and its connection to the torrent
205 prone to debris flows (Delaloye *et al.*, 2013; Kummert, Delaloye and Braillard, 2018). This offers a near
206 real-time visual check of the Grosse Grabe North pillar, detecting the first rockfall events in the winter
207 of 2017 and dating and locating the rockfall events thereafter, similar to D'Amato *et al.* (2016). The
208 automatic camera imagery also revealed that some parts of the pillar showed precursory deformation
209 before 2017 (Figure S1, Suppl. Material), but as the motion was mostly directed towards the camera,
210 it was not possible to quantify it reliably. The automatic camera is powered by an 80 W solar panel
211 which charges a 12 V battery. This battery is also used to power a router which transfers the hourly
212 images to a server. Near real-time images and selected time lapse sequences can be accessed via the
213 webpage of the Geomorphology research group of Fribourg University (*Study sites - Grosse Grabe*,
214 2021).



215
 216 **Figure 3.:** Set-up of the hourly terrestrial time-lapse photography: a) the installed automatic camera
 217 on a large boulder on stable bedrock and b) example of a photograph taken by the automatic camera,
 218 displaying the situation before the summer of 2019, indicating the unstable Grosse Grabe North Pillar
 219 (striped line), the location of the small scale 2017 rockfall (red circle) and the rock glaciers (blue lines)
 220 as the initial subject of study.

221
 222 *2.4. Detailed topographic data derived from terrestrial laser scans and Uncrewed Aerial Vehicle*
 223 *photographs*

224 Terrestrial laser scans (TLS) of the study area were performed from 2017 to 2020 at the beginning
 225 (late June/early July) and end (late September/early October) of the summer season (Table 1), using
 226 an ultra-long-range near-infrared pulse-based Riegl VZ[®]-6000 LiDAR system. This LiDAR system allows
 227 for a rapid survey (up to 222 000 measurements per second) and permits scans at a large distance from
 228 the area of interest (in this case ca. 700 m) (Figure 1). The TLS scan provides high-resolution 3-
 229 dimensional point cloud data from the upper talus slope, the upper rock glacier front, Grosse Grabe
 230 North Pillar and the adjacent rockwall (Figure 1 c). Starting in 2020, additional scans were executed at
 231 the same place to get topographic data from the lower part of the talus slope/rock glacier below to
 232 investigate the rockfall deposits. The resulting point clouds were post-processed in RiScanPro[®]
 233 software (version 3.3.438). Data were registered relatively to each other in a local coordinate system
 234 using the first scan of geomorphologically stable areas as a reference such as developed by Fischer *et*
 235 *al.* (2016) and Kummert and Delaloye (2018). The multi-station adjustment of all scans achieved an
 236 accuracy of 0.03 m as the overall standard deviation of the normal distances and is used as the Level

237 of Detection (LoD). The residuals of the corresponding stable areas between the reference scan
238 and the registered scan showed Gaussian distributions. The resulting point cloud was subsampled
239 to a minimum point spacing of 0.10 m using RiScanPro®'s octree filter.

240 Uncrewed Aerial Vehicle (UAV) photographs were gathered after large rock- and cliff fall events
241 in the summer of 2020 (Table 1) to improve the frequency of observations and to obtain observations
242 in areas not detectable from the TLS survey position due to topographic occlusion. The UAV imagery
243 was also used to make post-failure observations, allowing to visually detect if massive ice is present in
244 the rockfall scar. Five flights were performed with a DJI Phantom 4 Pro and flown without specific flight
245 planning. Given the inaccessibility of the site no ground control points were placed or measured. The
246 same software and workflow as in Hendrickx *et al.* (2020) were used for processing the photographs
247 into point clouds (See Suppl. Material for more details). To obtain data with high comparative accuracy,
248 the co-alignment methodology was adapted, based on the automatic detection of common tiepoints
249 in the stable areas. A small percentage of these common tiepoints (0.4 - 1%) is sufficient to enforce a
250 common geometry (Cook and Dietze, 2019). For Grosse Grabe, the five UAV surveys share 9% of the
251 total tiepoints. This resulted in a point cloud time-series with 0.30 m as the LoD, calculated on the
252 average change measured in the stable areas (Cook and Dietze, 2019), compared to 1-2 m of detected
253 change in the stable areas when the co-alignment method was not adopted. The resulting UAV derived
254 3D-models were used for the mapping and the measurements of the geological structures, using the
255 ShapeMetric3D software v3.7.1 (*ShapeMetric3D*, 2021).

256 Point clouds derived from TLS and UAV data were further analysed in CloudCompare (version
257 2.11). The Multiscale Model to Model Cloud Comparison (M3C2, normal and projection = 0.6 m,
258 calculated on all the points, minLoD as registration error, preferred orientation in -Y), developed by
259 Lague, Brodu and Leroux (2013), was used to quantify a 3D change accurately to detect deformation
260 of the rock face prior to any rockfall. The function "compute cloud/cloud distance" was used to quickly
261 identify rockfall zones. Both individual and cumulative rockfall volumes were calculated by fitting a
262 plane through the affected rock face and applying the resulting matrix values on the entire point cloud
263 using the 'Apply transformation tool'. This way, 2.5D volumes were calculated in the Z direction, taking
264 the LoD into account. When consecutive rockfall did not affect the same zone, rockfall volumes
265 from individual events could be derived from TLS/UAV data. Therefore, individual TLS volumes are
266 only available for the first rockfall events in the winter and spring of 2017 and 2018. Otherwise,
267 cumulative rockfall volumes spanning the monitoring interval were used to establish a relationship
268 between the measured seismic parameters. The total rockfall volume derived from the TLS data was
269 used to calculate rock wall erosion rate for the entire period of direct observation (2011-2021),
270 including observations from the automatic camera that confirmed no significant rockfall events
271 between 2011 and 2017. The resulting mean annual rockfall volume (m³) was divided by the slope-

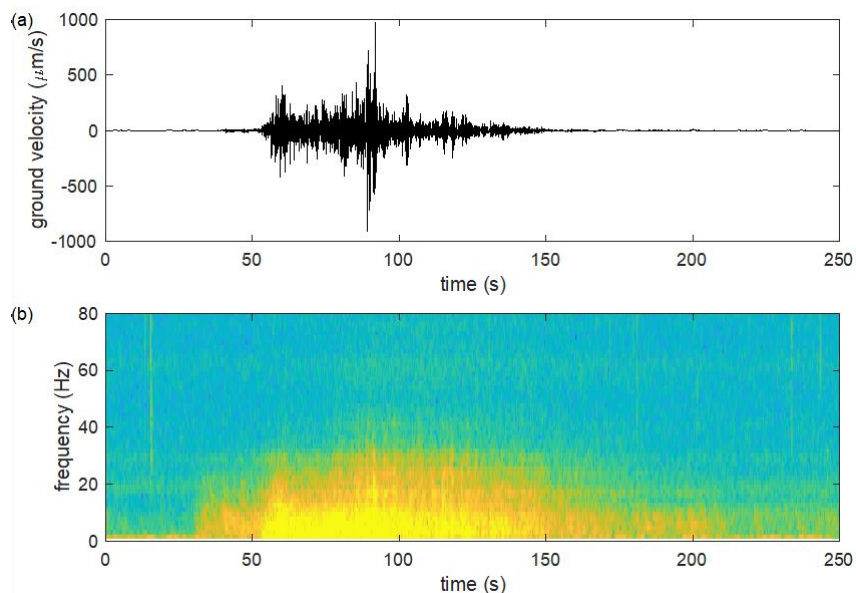
272 perpendicular surface area (m^2) of the studied rockwall (Figure 1 c, TLS extent), similar to the methods
273 used in Hartmeyer *et al.*, (2020).

274

275 2.5. Seismic observations

276 To obtain the exact timing of the rockfall events, we used seismic data of one seismometer
277 (Table 1), part of a network of six seismometers that have been installed to monitor Gugla rock glacier
278 (Guillemot *et al.*, 2020), located 2 km away from the rock face (Figure 1). This sensor was the only one
279 providing continuous data during this study (2017-2020). The sensor is a Sercel L22 one-component
280 geophone with a resonance frequency of 2 Hz (flat response above this frequency) and the signal is
281 recorded continuously at a sampling rate of 200 Hz since 2015. No significant rockfall was detected
282 from the study site before 2017.

283 We analysed all seismic events within the time interval of events detected by the automatic
284 camera. We selected all events with a peak ground velocity larger than $10 \mu\text{m s}^{-1}$ and characteristics
285 typical of rockfall seismic signals (Helmstetter and Garambois, 2010; Le Roy *et al.*, 2019): a duration
286 longer than 20 s and an energy content in the range 1-20 Hz. The seismic signal of the largest event is
287 shown in Figure 4. We also checked visually all signals to manually remove earthquake pulses, which
288 show a typical separate arrival of P- and S-wave and long-lasting decreasing tail (coda) (Dietze,
289 Turowski, *et al.*, 2017).



290

291 **Figure 4.** Seismogram (a) and spectrogram (b) for the largest event that occurred on 14 August 2020
292 at 10:59 UTC time.

293

294 We then estimated the seismic energy of each event assuming a point-source (Kanamori and
 295 Given, 1982; Eissler and Kanamori, 1987) because the source-sensor distance is much larger than the
 296 source area, considering the medium as isotropic and homogeneous. We also considered that surface
 297 waves dominate the seismic signal (Deparis *et al.*, 2008; Vilajosana *et al.*, 2008; Dammeier *et al.*, 2011).
 298 Signals were band-pass filtered between 2 and 20 Hz. We used the following relationship to estimate
 299 the seismic energy E_s (Vilajosana *et al.*, 2008):

$$300 \quad E_s = 2\pi r \rho h c \int_{t_0}^{t_1} u_{env}(t)^2 e^{\alpha r} dt \quad (1)$$

301 where t_0 and t_1 are the manually picked onset and end times of the seismic signal, r is the distance
 302 between the event and the recording station (2040 m for the North Pillar and 1400 m for the South
 303 Pillar), ρ is the ground density (assumed at 2700 kg m⁻³), h is the thickness of the layer through which
 304 surface waves propagate (taken as one wavelength of Rayleigh waves, $h=200$ m for a frequency
 305 centroid of 10 Hz), c is the phase velocity of Rayleigh waves (assumed at 2000 m s⁻¹), $u_{env}(t)$ is the
 306 envelope of the ground velocity obtained using the Hilbert transform. The damping factor α accounts
 307 for an elastic attenuation of seismic waves and is calculated using the maximum amplitudes of the
 308 rockfall seismic signal at two seismic stations and the distances between source and sensor. Since only
 309 one seismic station is available for the study site, the value (of $\alpha = 8.8 \times 10^{-4} \text{ m}^{-1}$) estimated for Mount
 310 Saint-Eynard rockfalls was used, with a frequency centroid of 10 Hz (Le Roy *et al.*, 2019).

311 Rockfall seismic signals can also be characterized by their equivalent magnitude, using the
 312 same relations as for earthquakes. Local magnitude can be estimated from the seismic energy using
 313 the Gutenberg-Richter magnitude-energy relation (Kanamori and Anderson, 1975).

$$314 \quad \text{Log } E_s = 1.5M_L + 4.8 \quad (2)$$

315 We then calibrated a relation between the magnitude M_L of a rockfall event and its volume V . We
 316 assumed a relation in the form of (Le Roy *et al.*, 2019):

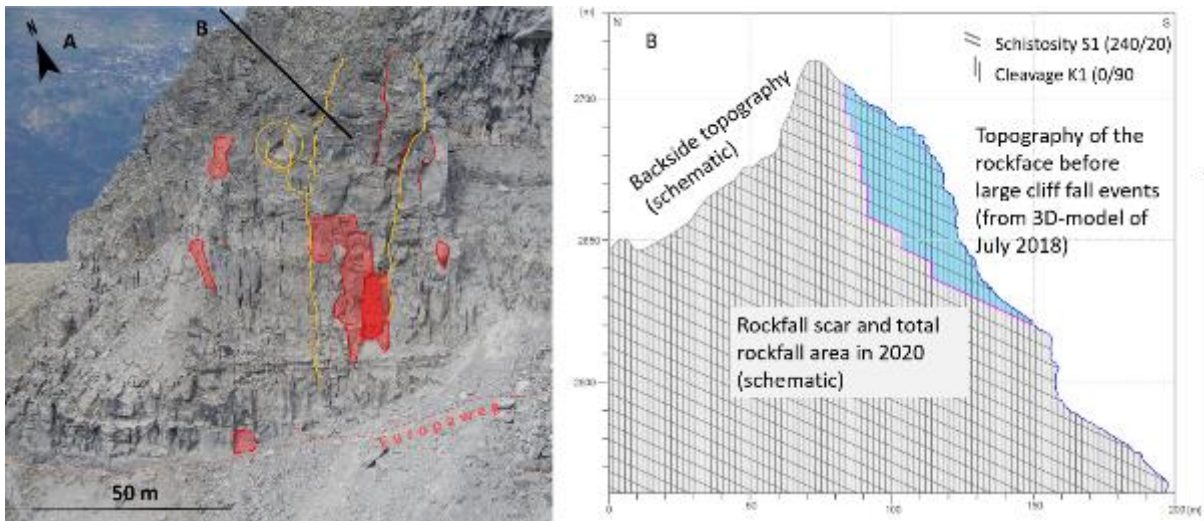
$$317 \quad M_L = a \log_{10}(V) - b \quad (3)$$

318 For each time interval between two TLS or UAV surveys, we selected all events within this time interval.
 319 We then optimized the parameters a and b of equation (3) in order to minimize the root-mean-square
 320 error between the logarithm of volume estimated from TLS or UAV surveys and the cumulated volume
 321 estimated from the signal magnitude using equation (3). We found $a=0.84$ and $b=1.38$, in good
 322 agreement with the results obtained by Le Roy *et al.* (2019) for rockfalls in the Chartreuse massif
 323 (French Alps).

324

325 3. Results

327



328

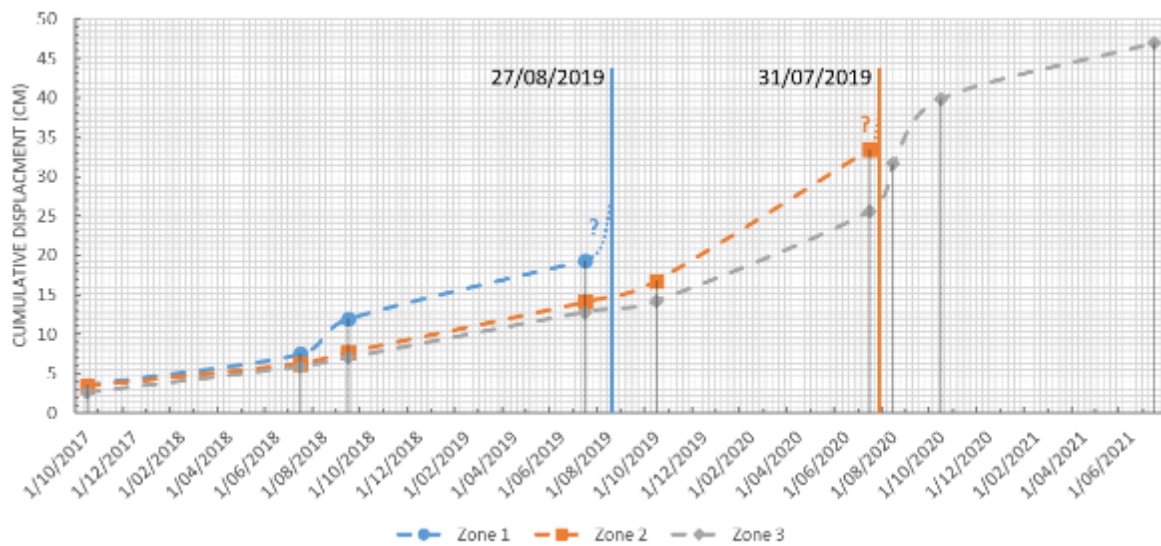
329 **Figure 5.** Close up of Grosse Grabe North Pillar: a) Before any large rockfall occurred (photograph of
 330 06/09/2018). Precursory indicators of destabilization could already be observed by terrestrial laser
 331 scanner (red) and automatic camera (yellow) in forms of small scale rockfall ($< 10^3 \text{ m}^3$) and fracture
 332 opening. And b) geological cross section showing main schistosity and cleavage related to the total
 333 rockfall area and scar surface (derived from ShapeMetric3D software).

334

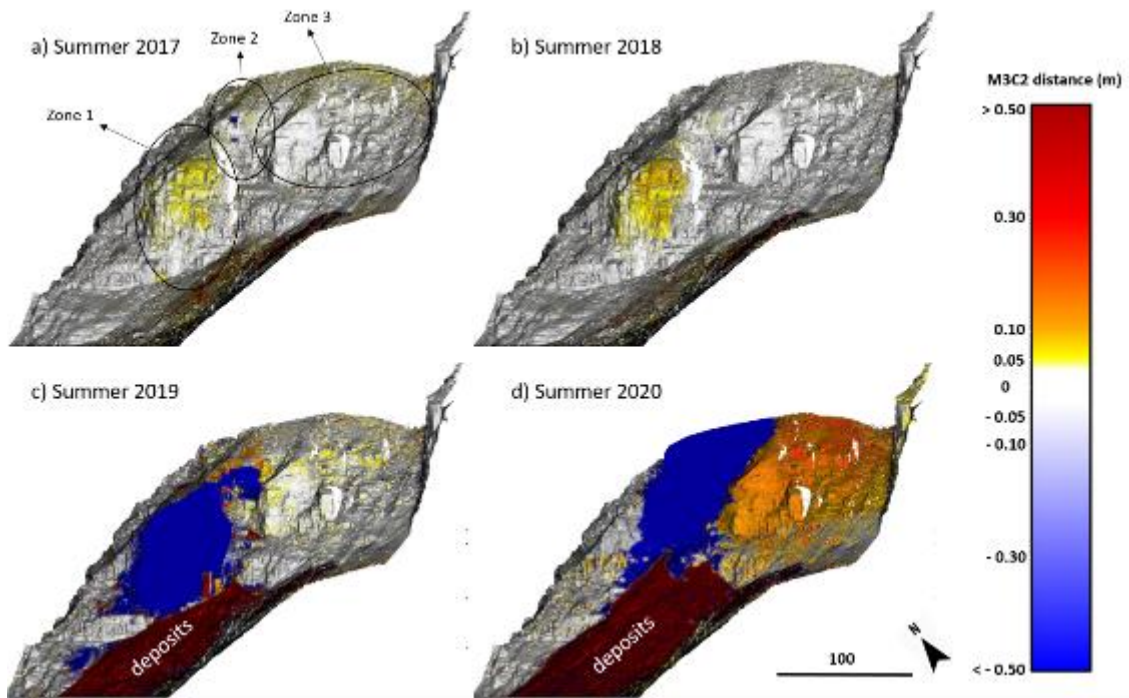
335 Two isolated boulder falls (10^1 - 10^2 m^3) were detected visually for the first time in January and May
 336 2017 (Figure 3b, Figure 5 a, yellow circle), launching a more accurate survey of Grosse Grabe North
 337 Pillar and the adjacent rock wall by Terrestrial laser scans (TLS) in July 2017. In the following winter
 338 seasons of 2018 and 2019, small magnitude rockfall ($< 10^3 \text{ m}^3$) were observed, occurring in between
 339 January and May (Figure 5 a, red polygons). In the summer of 2019 and 2020 larger magnitude rockfalls
 340 (10^4 m^3) and cliff falls (10^4 - 10^6 m^3) followed up each other in close succession, with no single
 341 rockfall event in the associated winter period (November 2019 – April 2020).

342 Besides rockfall, deformation of the Grosse Grabe North Pillar was also observed as an outward
 343 displacement with more pronounced displacement in the upper part, indicating a tilting or toppling
 344 motion. Cleft opening and widening, associated with this outward displacement, could be observed on
 345 two different time scales. TLS data indicated that cleft opening at the upper part of the rock pillar was
 346 already ongoing in 2017 and 2018, gradually opening up (Figure 5 a, red lines), while automatic camera
 347 imagery revealed an accelerated cleft widening four to five weeks before the first cliff fall in August
 348 2019 (Figure 5 a, yellow lines, Figure S2, suppl. material). The observed displacement and associated
 349 cleft opening is therefore considered to be the main precursory factor for the sudden large rock- and
 350 cliff fall events having occurred in the summer of 2019 and 2020. The observed displacement also has

351 a clear seasonal pattern with an average monthly displacement by a factor of 1.2 to 2 times bigger in
 352 summer (June-September) than in winter (October-May) (Figure 6). Three different zones can be
 353 distinguished (Figure 6, 7, 8): (i) zone 1 that collapsed in the summer of 2019 (Figure 7 c, Figure 8 b),
 354 and corresponds to the Grosse Grabe North Pillar, displayed on Figure 5, (ii) zone 2 that collapsed
 355 almost entirely in the summer of 2020 (Figure 7 d, Figure 8 c,d) and (iii) zone 3 that has not yet
 356 experienced any large rockfall up to the summer of 2021 (Figure 7 d, Figure 8 d). However, rockfall is
 357 still to be expected in this zone, where a cumulative displacement of up to 47 cm has been (Figure 6,
 358 7 d).
 359



360
 361 **Figure 6.:** Cumulative displacement based on the third quartile (75th percentile) of all the measured
 362 displacement for Grosse Grabe North Pillar (Zone 1) and the adjacent rock face (zone 2 and zone 3).
 363 Collapse date is indicated for zone 1 and 2, while zone 3 has not experienced any significant rockfall
 364 up to the summer of 2021. Dotted line is an interpolation of the measurements.
 365

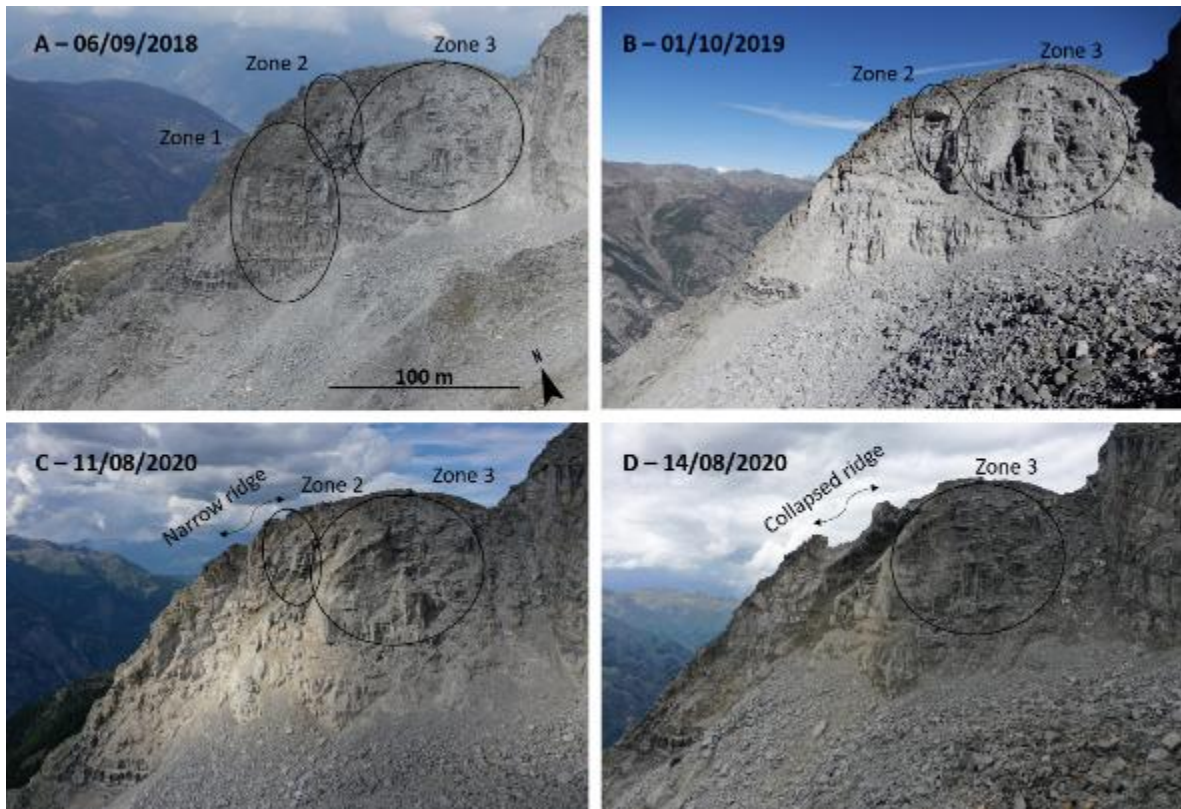


366

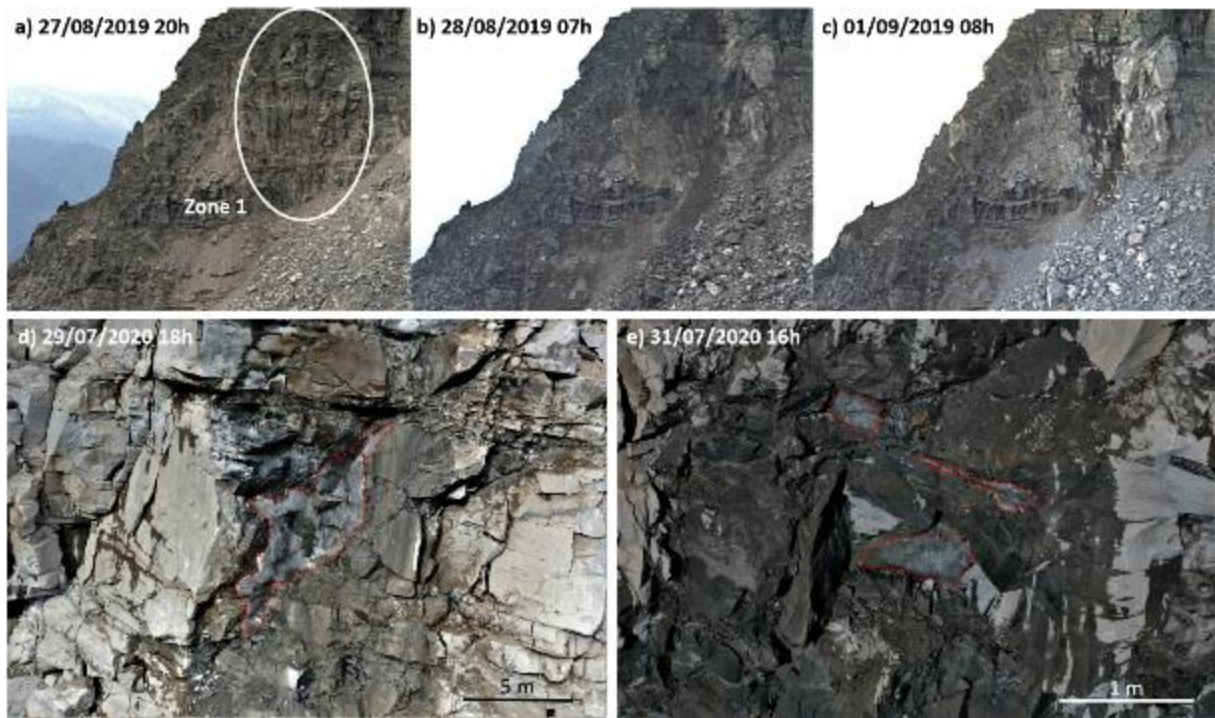
367 **Figure 7.:** The forward displacement of the Grosse Grabe North Pillar (zone 1) and adjacent rock
 368 wall (zone 2 and 3) in the summer of a) 2017, b) 2018, c) 2019 and d) 2020. Observed changes are
 369 relative to the scan at the beginning of summer and are statistically significant at the 95% confidence
 370 level with a minimum level of detection of 3 cm. Background is a hillshade based on terrestrial laser
 371 scan surveys.

372 A wet rockfall scar was observed by the automatic camera for several days after large cliff
 373 falls, in otherwise dry conditions, suggesting the presence of ice and thus potentially thawing
 374 permafrost. This was observed for the first time at the end of August 2019, when a total scar
 375 depth of 22.5 m (Figure 5 b), measured by the TLS data, was reached from the precluding rock-
 376 and cliff fall events (Figure 9 a). In the summer of 2020, the presence of compact ice could be
 377 confirmed with more detailed UAV imagery (Figure 9 b, c) after fresh rock- and cliff fall events
 378 occurring on 29 July and 31 July 2020 respectively. The latter was a very large cliff failure, with a
 379 calculated volume of $21\,392 \pm 6418 \text{ m}^3$ based on the UAV imagery (Video S1; Suppl. Material).
 380 Following rockfall events (Table 2) diminished the width of the upper ridge even further by
 381 removing 17.1 m of rock. This resulted in a very narrow and highly fractured ridge of a width of
 382 only 8 m, as calculated by using the UAV imagery (Figure 8 c). Finally, the ridge collapsed after
 383 several large rock- and cliff fall events that took place on 14 August 2020 between 8h30 and 11h,
 384 accounting for the largest volume of $33\,880 \pm 10164 \text{ m}^3$ recorded so far (Table 2, Figure 8 d). A
 385 laser scan performed on the 19 August 2020 measured a total volume of $94\,523 \pm 3781 \text{ m}^3$ for
 386 the entire summer period (01 July – 19 August 2020), this being an underestimation because no

387 surface comparison could be made where the ridge was denudated (estimated to have had a
388 volume of $\pm 3000 \text{ m}^3$ based on the seismic signal and thus within the error margin of the TLS
389 derived volume).



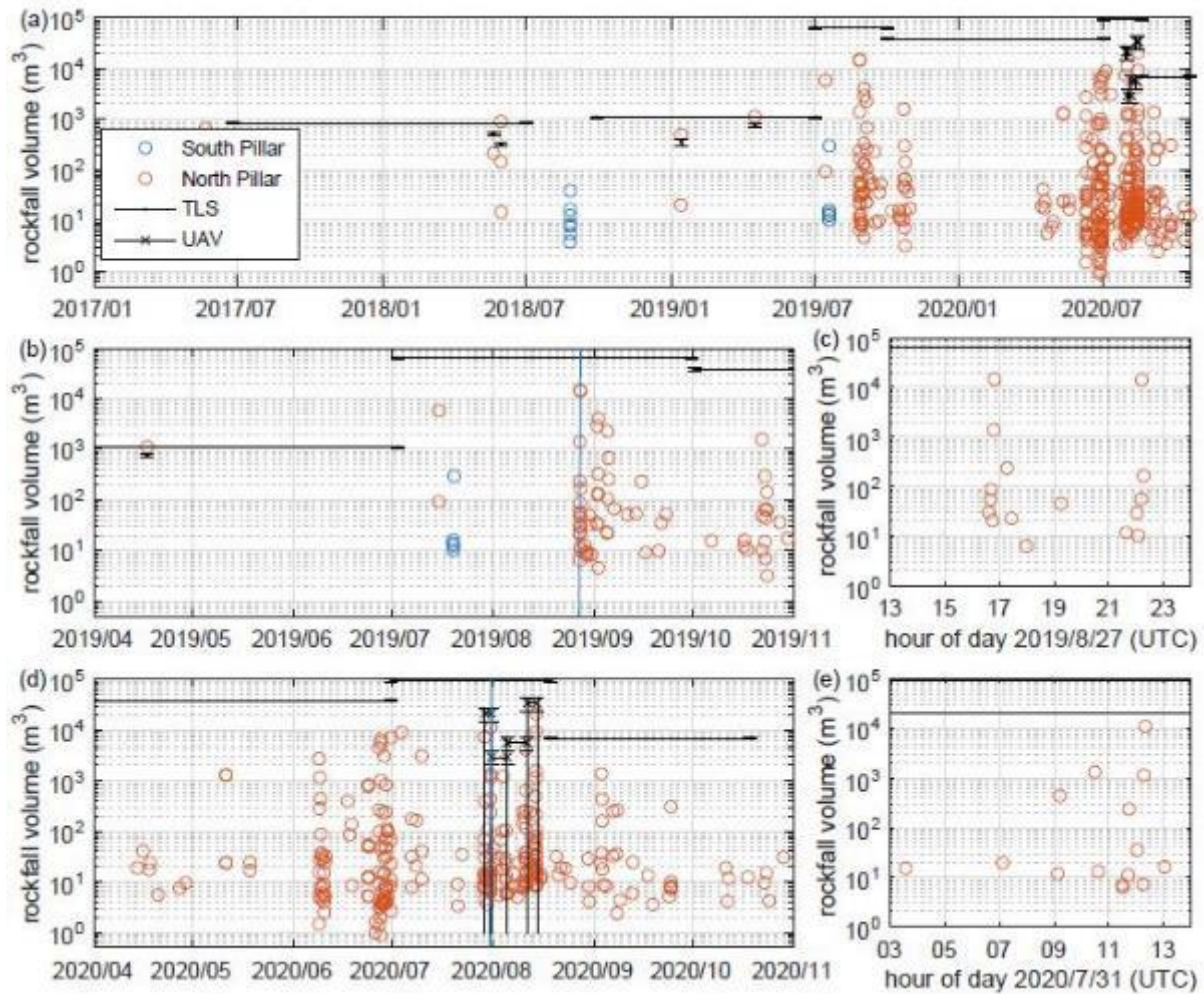
390
391 **Figure 8:** Geomorphological development of Grosse Grabe North Pillar and the adjacent rock
392 wall: a) Situation before the large rock- and cliff fall events of the summer of 2019 and b) after
393 the summer of 2019 and the situation c) before and d) after the largest cliff fall event on 14
394 August 2020, causing the collapse of part of the ridge. All imagery taken under a (sub-
395)horizontal angle.
396



397
 398 **Figure 9.:** Exposed ice at Grosse Grabe North Pillar (Zone 1), indicating the possible presence of
 399 permafrost, which occurs deep in the rock face following a cliff fall event, a) automatic camera
 400 imagery of 2019 showing an image before and b) after the cliff fall event of 27 August 2019, and
 401 c) the wet rockfall scar a couple of days after in otherwise dry conditions, d) UAV imagery shortly
 402 after the event of 29 July 2020 showing compacted ice and e) UAV imagery after the event of 31
 403 July 2020 showing smaller ice patches, indicated by a red dotted line. All imagery taken under a
 404 (sub-)horizontal angle.

405
 406

407 *3.2. The timing and extent of rockfall events*



408

409 **Figure 10.:** Timeline of rockfall events (a) for the full time period between January 2017 and
 410 September 2020, (b) for the period April 2019 – November 2019, with c) highlighting the first
 411 large cliff fall events on 27/08/2019, d) for the period April 2020 – November 2020, with e)
 412 highlighting the cliff fall event on 31/07/2020, showing precursory rockfall. Red (North Pillar) and
 413 Blue (South Pillar) circles represent individual rockfall volumes estimated from the seismic signals
 414 using equations (1-3). Black dots and black crosses represent respectively cumulated volumes in
 415 each time interval between TLS or UAV surveys.

416

417 **Table 2.:** The topographic data gathered and the resulting rockfall volumes calculated

Date (dd/mm/yyyy)	Topographic data derived from:	Number of scans or photographs	Number of points in point cloud	Rockfall volumes since previous survey (m ³)	Cumulated volume from seismic signals (m ³) (95% confidence interval)
26/06/2017	TLS	1	15 500 167		
06/10/2017	TLS	1	16 313 071	0	0
03/07/2018	TLS	1	20 191 249	831 ± 33	1265 (416-3845)
29/09/2018	TLS	1	18 350 987	0	92 (30-281)

03/07/2019	TLS	1	13 628 608	1 102 ± 44	1635	(538-4969)
01/10/2019	TLS	1	20 566 426	63 138 ± 2526	49 192	(16181-149548)
01/07/2020	TLS	2	32 640 662	37 697 ± 1508	42 466	(13969-129102)
19/08/2020	TLS	2	24 300 449	94 523 ± 3781	76 991	(25325-234061)
19/10/2020	TLS	2	38 576 084	6846 ± 274	3208	(1055-9752)
29/07/2020	UAV	139	21 045 119			
31/07/2020	UAV	79	21 208 056	21 392 ± 6418	59 779	(19663-181734)
05/08/2020	UAV	116	16 630 783	2 880 ± 864	6025	(1982-18317)
11/08/2020	UAV	139	18 593 781	5 559 ± 1668	6025	(1982-18317)
14/08/2020	UAV	149	14 383 741	33 880 ± 10164	34 260	(11269-104155)
Total measured volume (26/06/2017-19/10/2020)				204 137 ± 8166	175700	(57794-534147)

418 TLS: terrestrial laser scanning, UAV: uncrewed aerial vehicle

419

420 Analysing the seismic data resulted in a high temporal record of all the rock- and cliff fall
421 events that occurred at Grosse Grabe North pillar and adjacent rock wall. The few events that
422 occurred at Grosse Grabe South Pillar, out of reach for the automatic camera and the TLS/UAV
423 data could also be quantified. In total, the seismic logger detected 339 rockfall events for the
424 North Pillar and 12 for the South Pillar in the timespan of four years (2017-2020) (Figure 10)
425 (Table S1, Suppl. Material). Most of the timely isolated and significant events at the North Pillar
426 could be confirmed by the automatic camera, indicating the zone of failure (Figure S2, Suppl.
427 Material). Isolated and small scale rockfall events occurred before the summer of 2019, in mid-
428 winter (January) and in springtime (April - May). This changed in the summer of 2019, with the
429 first isolated larger rockfall event occurring in mid-July ($10^3 - 10^4 \text{ m}^3$) precluding larger cliff fall
430 events (10^4 m^3) around the end of August (Figure 10 b, c). Rockfall continued to occur throughout
431 September and October, but decreasing in magnitude (Figure 10 b). No rockfall occurred during
432 the winter of 2019-2020 (November – May). Rockfall events started again in April-May 2020
433 (Figure 10 d). By the end of June and throughout July and August several cliff fall events (10^4 m^3)
434 were observed again (Figure 10 d, e). The last event of around 500 m^3 occurred in late October.
435 No significant rockfall events were observed in the following winter (2020-2021). It can be
436 deduced from the seismic dataset (Figure 10) that 82% of the larger rock- and cliff fall events (> 5000
437 m^3 , $N=11$) are precluded by two or more smaller events. In all cases, precursory rockfall happened
438 within the hour before a large failure, often only a few minutes before. Only half of the larger rockfall
439 events experienced precursory rockfall several hours before (Figure 10 e). Post-failure small-scale
440 boulder falls ($\leq 10^2 \text{ m}^3$) happened some minutes up to a few hours after the collapse are common as
441 well (Figure 10 c). After that, rockfall activity ceased for several days up to weeks before rockfall events
442 became numerous again ($\leq 10^3 \text{ m}^3$). At the same time, these events announced the detachment of
443 the next larger volumes of rockfall. This process continued until late summer, when finally rockfall
444 activity ceased until spring.

445 The cross correlation between the meteorological data (temperature and precipitation)
446 and rockfall activity suggests that rockfall occurs more frequently a few days after precipitation
447 or a warming event, but the correlation is very weak (peak correlation of around 0.1 for daily
448 precipitation for a time delay of 2 days) and barely significant. This could be because of the short
449 time dataset (2017 – 2020), where the events are grouped together in burst of activities.
450 However, it is clear that rockfall activity mostly develops in the summer only (Figure 10). Half of
451 the large rock- and cliff fall events we observed happened in the second half of the summer (end
452 of July, August), when temperatures are in general warmer and when summer air temperature
453 had the time to warm the rock temperature at depth. Moreover, most large rock- and cliff fall (8
454 out of 11) occurred in the (late) afternoon. In addition, the three rockfall events that occurred in
455 June 2020 were precluded by weekly higher temperatures (7.9 ± 0.3 °C) than are the average for
456 June (5.7 ± 2.7 °C) based on data of the PermaSense weather station (2013-2020). This is also the
457 case with the four large rockfall events between 29 July – 14 August 2020, precluded by
458 significantly higher temperatures (10.5 ± 1.2 °C) than normal for that time of the year (7.8 ± 1.5
459 °C).

460

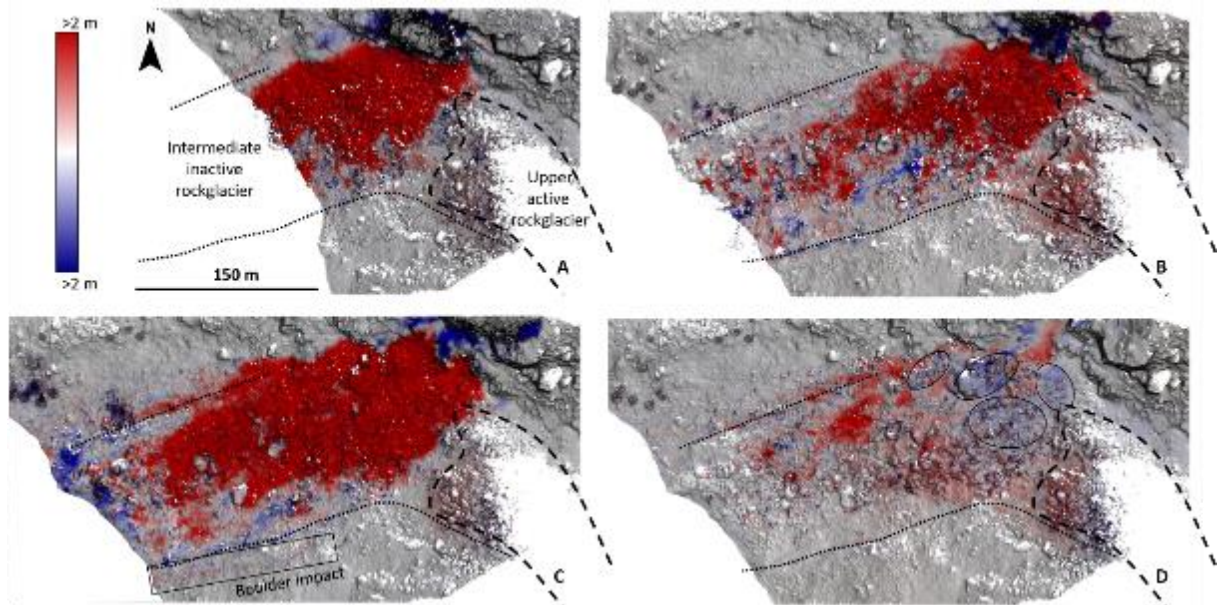
461 3.3. Rockwall erosion rates and the deposited material

462 A total rockfall volume of $204\,137 \pm 8166$ m³ was measured based on high resolution TLS and
463 UAV derived topographic data (Table 2, 2017-2020). Since no significant rockfall was observed by the
464 automatic camera since 2011, we assume this to be the total rockfall volume across a full 10-year
465 period of direct observations. This corresponds to a mean rockwall erosion rate of 214 ± 8.9 mm a⁻¹ for
466 Grosse Grabe North Pillar and the adjacent rockwall (Figure 1 c, TLS extent). If we include the indirect
467 observations of rockfall occurrence based on historical aerial photographs (Figure 2), we can assume
468 that the measured rockfall volume (2017-2020) was the only significant rockfall across a 30-year
469 period. This would correspond to a mean rockwall erosion rate of 71.2 ± 2.8 mm a⁻¹.

470 More than 200 000 m³ of material was deposited below the Grosse Grabe North Pillar in
471 between 2017 and 2020, based on the measured and estimated rockfall volumes. These deposits
472 overlay most of the intermediate rupture zone between the upper intact part and the terminal tongue
473 of the Grosse Grabe rock glacier (Figure 2). The measured deposited volumes within the range of
474 the TLS scan (Figure 11) are $99\,625 \pm 3985$ m³ for 2019-2020. If we assume an initial porosity of
475 30%, in line with the porosity of blocky talus (Sass and Wollny, 2001) and that of other rockfall
476 deposits in an alpine setting (Sanders *et al.*, 2013), we get an estimated deposited volume of 70
477 000 m³. As settling of the deposit sets in, a downward movement of up to two meters could be

478 observed in late summer – autumn 2020 at the apex of the rock fall deposit cone. The motion is
479 restricted to the deposited area and is diminishing further down, indicating crushing and a
480 decrease in porosity as main process for the movement caused (Figure 11). Single large boulders
481 were also transported into the Grosse Grabe torrent, outside the range of the scan (Video S1;
482 Suppl. material). This occurred at least 11 times according to the imagery of the automatic
483 camera, corresponding with the largest rock- and cliff fall events ($> 5000 \text{ m}^3$) during the summer
484 of 2019 and 2020. Rock debris is considered ending up in the torrent each time it is discernibly
485 overpassing the rock glacier front.

486



487

488 **Figure 11.:** Rockfall deposits (thickness perpendicular to slope) on the talus slope below the
489 rock face for a) the summer of 2019, b) the winter of 2019-2020, c) the first part of the summer
490 of 2020 (1 July – 19 August) and d) the second part of the summer of 2020 (19 August – 19
491 October), the latter showing compression of the deposits under their own weight in the upper
492 part of the debris cone (indicated by the ellipses). Zones with no data is due to differences in
493 the scan extent.

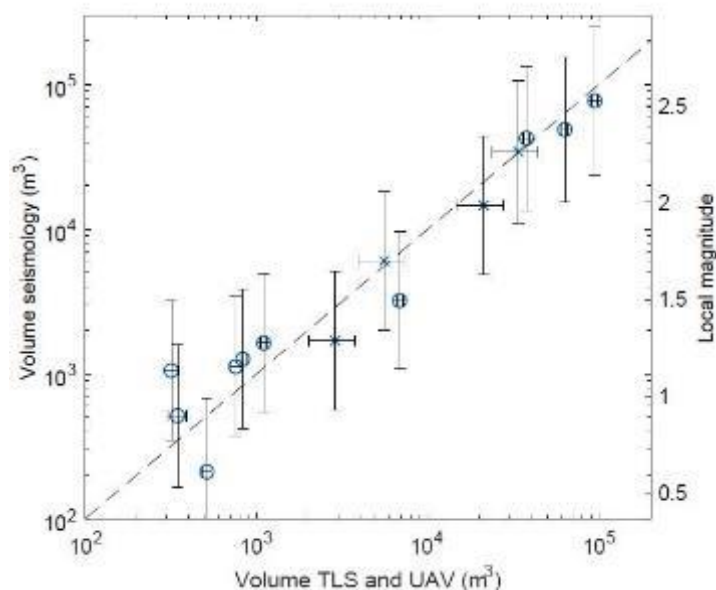
494

495 4. Discussion

496 4.1. Limitations of the methods

497 Uncertainties remain present within the collected high resolution datasets, even though different
498 methods were integrated and the record starts two years prior to the main destabilisation period. The
499 TLS data serves well to detect and quantify precursory deformation before the large rockfall events in

500 the summer of 2019 and 2020 but was limited to a Level Of Detection (LoD) of 3 cm and the monitoring
501 interval. Precursory deformation in zone 2 and 3 was close to this LoD at the onset of the monitoring
502 period (Figure 6). (Near-) continuous and more detailed quantification of rockwall deformation and
503 cleft opening can alternatively be achieved by ground-based InSAR (Gischig *et al.*, 2009) and the in-situ
504 installation of crackmeters (Weber *et al.*, 2017). However, such methods are expensive and depend
505 highly on site accessibility respectively. Imagery from the time-lapse camera was also able to detect
506 the outward movement, already occurring before 2017 (Figure S1, Suppl. Material), but could only be
507 quantified after the launch of the TLS survey. From the additional scan performed in August 2020, we
508 know that the largest displacement occurs at the end of the summer season (19/08-19/10/2020). The
509 measured winter (October – May) displacement likely occurs mostly in autumn, although this cannot
510 be confirmed due to the restrictions of the monitoring interval. The monitoring interval does not allow
511 rockfall volumes to be calculated either if they were released from the same zone. The largest rockfall
512 events also caused topographic occlusion due to the single scan position, leading to an
513 underestimation of the rockfall volume. This is somewhat corrected by the five UAV surveys launched
514 before and after the largest events in the summer of 2020, not suffering from occlusion. However, the
515 occluded volumes, calculated by subtracting the UAV derived volumes with the TLS derived volumes,
516 fall completely within the error margins of the TLS data (< 4 – 5 %) and would thus not affect the
517 results significantly. Besides the visual confirmation of ice in the rockfall scars only hours after the
518 events, this shorter monitoring interval also allows the optimising of the established relationship
519 between measured volumes and the seismic signal (Figure 12). Overall, we achieve a good fit between
520 the estimated volume based on the seismic data and the ones more directly measured by TLS and UAV
521 point cloud meshes (Table 2). The seismic data collection is the only monitoring method in this study
522 that allows all rockfall events to be recorded. This way, pre- and post-event rockfall events could be
523 analysed. The seismic data of only one sensor could be used for the rockfall period. This has the
524 disadvantage that rockfall locations cannot be estimated precisely. It is therefore crucial to have the
525 time-lapse imagery to validate the observed seismic signals. Only one event with a large amplitude was
526 recorded by the seismic sensor and could not be detected on the time-lapse imagery. Likely, this
527 rockfall event with an estimated volume of 300 m³ occurred elsewhere in the area.



528
 529 **Figure 12.** Volume estimated from the seismic signals and equivalent local magnitude as a function of
 530 rockfall volume estimated from TLS (circles) or UAV surveys (crosses) (summing over all events in each
 531 time interval). Error bars are 95% confidence intervals given by a linear fit of logarithms of volumes.

532
 533 *4.2. Structural predisposition, potential preparatory factors and observed precursory indicators to*
 534 *rock slope destabilisation*

535 At Grosse Grabe North Pillar, the gentle dipping angle of 20° and cleavage-parallel weak layers
 536 susceptible to disruption in combination with deep, persistent and sub-vertical fracture systems favour
 537 large rockfalls (Figure 5 b). Already in 1982 and the following years, similar consecutive events took
 538 place (Figure 2). Probably the same structural conditions were at play. This could be a geological legacy
 539 of the glacial retreat after the Last Glacial Maximum, known to have affected and cause rock fractures
 540 in the Matter Valley (Leith *et al.*, 2014). The structural predisposition of the studied rock face entails
 541 several potential failure mechanisms, acting on fracture level, to operate as preparatory factors.
 542 Irreversible movements of fractures can be caused by thermal fluctuations (Gunzburger, Merrien-
 543 Soukatchoff and Guglielmi, 2005; Collins and Stock, 2016; Bakun-Mazor *et al.*, 2020), water pressure
 544 (Hasler, Gruber and Beutel, 2012; Walter *et al.*, 2019), freezing and thawing of water in the rock mass
 545 (Hasler, Gruber and Beutel, 2012; Weber *et al.*, 2017) and seismic vibrations (Luckman, 2013; Bakun-
 546 Mazor *et al.*, 2020) and a combination of all of these processes.

547 The cumulative and repetitive nature of thermally induced failure mechanisms are considered
 548 an important preparatory factor for rockfall in fractured rock masses exposed to high temperature
 549 oscillations (Gunzburger, Merrien-Soukatchoff and Guglielmi, 2005; Collins and Stock, 2016; Draebing,
 550 Krautblatter and Hoffmann, 2017; Bakun-Mazor *et al.*, 2020). Although no in situ rock temperatures

551 were measured at the south facing rock face of Grosse Grabe, similar south-exposed rockwalls yield a
552 daily temperature variation of up to 16.5°C compared to only 4°C for north-facing rockwalls as a result
553 of solar radiation differences (Draebing and Mayer, 2021). While daily temperature changes only
554 penetrate down to shallow depths (up to 0.4 m) (Gunzburger, Merrien-Soukatchoff and Guglielmi,
555 2005), seasonal thermal changes can propagate deeper in highly fractured bedrock (up to 100 m) due
556 to air convection (Gischig *et al.*, 2011). Thus, Grosse Grabe North pillar is likely to be very susceptible
557 to this thermally induced failure mechanism due to large daily and seasonal temperature variations,
558 the presence of a gently inclined sliding plane and the high fracture density of the rock (Figure 5 b).
559 Moreover, such thermally induced displacements are typically observed when temperatures are rising
560 during summer (Bakun-Mazor *et al.*, 2020). This matches well with the observed seasonality of the pre-
561 failure displacement observed at Grosse Grabe, with a displacement that was more pronounced by a
562 factor of 1.2 to 2 in summer (Figure 6, 7). The observed larger irreversible displacements in summer
563 might also indicate the potential role of water-related processes, such as changes in water pressure
564 (Walter *et al.*, 2019) and advective warming by water percolation (Hasler *et al.*, 2011; Weber *et al.*,
565 2017), for example due to snow or permafrost meltwater (Weber *et al.*, 2017) and summer rainfall
566 (Walter *et al.*, 2019). However, we found no indication for the latter in the meteorological data,
567 possibly due to the long offset-time until rockfall occurrence. In addition, the catchment area of the
568 rock face is small and mostly free of snow. Moreover, water pressure might not be dominant in strongly
569 fractured and steep rock because of its high drainage ability (Phillips *et al.*, 2016; Weber *et al.*, 2017).
570 Seismic vibrations due to earthquakes might influence fracture stability and prepare and trigger
571 rockfall (Luckman, 2013). 2634 earthquake events were measured by the seismic sensor since 2015
572 and this might have played a role in rock wall destabilisation. However, the earthquakes observed for
573 our analysed period never exceeded a ground motion of 2 mm s^{-1} , too weak to trigger any rockfall as
574 compared to a ground motion 0.5 m s^{-1} suggested as a minimum threshold for triggering landslides or
575 rockfalls (Keefer, 1984).

576 Temperature cycles also drive cryogenic processes in the studied rock wall, due the confirmed
577 presence of ice (Figure 9). Although observed winter rockfall activity is limited, frost weathering can
578 still act as a preparatory factor for rockfall occurrence by subcritical cracking and progressively
579 reducing rock strength (Draebing and Krautblatter, 2019). Frost weathering might be highly effective
580 at Grosse Grabe North Pillar, as indicated by modelling results of rock walls at similar elevation and
581 exposition (Draebing and Mayer, 2021), preparing rockfall that is than subsequently triggered by
582 processes in summer, such as thermal stresses described above. Fracture displacement due to
583 cryogenic processes is often linked to ice pressure and thus widening of the fractures at the onset of
584 freezing (Draebing, Krautblatter and Hoffmann, 2017; Weber *et al.*, 2017). However, we observed a
585 decrease in the displacement in winter, which we link to the cementing effect of permanent and

586 seasonal ice as a consequence of a rapid cooling of the clefts due to colder air temperatures and
587 probably to air circulation in the fractured rock (Gruber and Haeberli, 2007; Hasler, Gruber and Beutel,
588 2012). This cementing effect of the ice-bonded discontinuities decreases progressively during the
589 summer due to a decrease in stiffness and strength of the ice at warmer temperatures (Davies, Hamza
590 and Harris, 2001). This hypothesis is supported by the presence of ice in the deeper bedrock (at least
591 at 15 m depth), affecting the sub-vertical fractures. Permafrost degradation might therefore be a
592 potential preparatory factor, considering the long-term warming of the area.

593 Both precursory rockfall and deformation are known to sometimes prelude rock- and cliff fall
594 (Abellán *et al.*, 2010). From the moment fractures are subjected to large irreversible movements,
595 driven by one or several of the mechanisms explained above, a critical state will slowly be reached
596 (Hasler, Gruber and Beutel, 2012). A change in deformation geometry is detected approx. 1.5 years
597 before the first significant collapse in zone 1 and zone 2. After this, large, irreversible movements are
598 clearly observed at Grosse Grabe North Pillar, with an increase in pre-failure displacement by a factor
599 of 2-3.5 prior to the collapse (Figure 6). This increase in outward displacement is mainly observed in
600 the upper part of Grosse Grabe North Pillar, with the rock volume staying the same, indicating a tilting
601 or toppling type of failure developed (Abellán *et al.*, 2010). This type of failure is often linked to sub-
602 vertical fractures (Goodman and Kieffer, 2000). At Grosse Grabe, the failure of sub-vertical fractures
603 in the lower rockwall are believed to be the cause of the toppling motion. The isolated rockfall events
604 before 27 August 2019 are considered to be precursory rockfalls precluding the destabilisation phase in
605 the summer of 2019 and 2020.

606 *4.3. Potential triggers leading to progressive rockwall collapse*

607 Most rockfall occurred in the warmer half of the year and no large rockfall occurred in winter.
608 In addition, large follow-up rockfall events (> 5000 m³) occurred when weekly temperatures were
609 warmer than average for that time of the year and occurred mostly in the (late) afternoon. Next to
610 thermal stresses, this could also indicate that the melting of ice-filled joints (or decreasing of their
611 resistance to stress) (Davies, Hamza and Harris, 2001) close to the surface plays a role. The depth
612 at which temperature change is perceptible in bedrock after a week of unusually high
613 temperature is likely to be no more than 1 m based on borehole data (PERMOS, 2016). Moreover,
614 larger events within this destabilisation phase were also announced by small-scale rockfall within hours
615 of the larger volume, similar to small magnitude rockfall events during hot summers (Figure 10 e).
616 These rockfall events are typically associated to permafrost presence at shallow depths, triggered by
617 active layer thickening (Ravanel, Magnin and Deline, 2017). Such type of rockfall had not been
618 observed at Grosse Grabe before the rockfall event of 27 August 2019 (Figure 10 c), indicating that
619 permafrost was not present at the sub-surface of the south-facing rock, confirming model results

620 (Boeckli *et al.*, 2012; Magnin *et al.*, 2017). However, permafrost presence was confirmed when
621 rockfall exposed massive ice (Figure 9), which often occurs after failures in permafrost-affected rock
622 (Gruber and Haeberli, 2007; Mamot *et al.*, 2018; Kenner, Bühler, *et al.*, 2019; Walter *et al.*, 2019).
623 According to numerical models of subsurface temperature fields in ridge topography (Noetzli *et al.*,
624 2007), this likely corresponds to the base of the permafrost developed at the north face, at the distance
625 of 50 – 70 m. We exclude the possibility that this is seasonal ice, considering it is exposed at the time
626 when we at least expect seasonal ice to persist (at the end of summer). Since the large cliff fall on 27
627 August 2019 (Figure 10 c) permafrost has been exposed and prone to rapid degradation due to thermal
628 adjustment and subsequent active layer thaw. This thermal adjustment, together with the
629 redistribution of stress from preceding large rockfalls (Nishii and Matsuoka, 2012; Stock *et al.*, 2012),
630 leads to progressive failure of the rock face and the observed rapid sequence of events (Figure 10).
631 The bounding ice quickly melted, not only at the surface but also at shallow depths in the clefts, quickly
632 changing the strength of the rock mass and favouring the detachment of the next volume. This process
633 did not occur in winter and ceased in September 2019, when cold weather conditions kept the exposed
634 face frozen and thus dry. Large rockfall events are to be expected for the next years at Grosse Grabe
635 North pillar, because of the dense fracturation of the rock face and the observed pre-failure
636 displacement of up to 47 cm in zone 3 (Figure 6, 7). However, no change in geometry (i.e. cleft
637 widening) has been observed in this zone. The displacement is characterised by a homogenous
638 movement of the face along the dipping plane, suggesting a deep-seated gravitational deformation or
639 sacking taking place.

640

641 4.4. Observed rock wall erosion rates and their implication for future development

642 High magnitude rockfall events, such as observed in this study, are highly relevant for shaping
643 alpine landscapes (McColl and Draebing, 2019). Logically, observations of rock wall retreat made in a
644 period of high rockfall activity tend to overestimate long-term rock wall erosion rates. Erosion rates
645 based on a short term record should therefore be interpreted with care (Hartmeyer *et al.*, 2020).
646 Commonly, long-term rock wall retreat rates for alpine periglacial environments are around 1 mm a^{-1}
647 (Ballantyne, 2018; Matsuoka, 2019). Higher rates are reported in deglaciating cirques, with a rate of
648 1.9 mm a^{-1} to 10.3 mm a^{-1} on short time scales (4-6 yrs) (Kenner *et al.*, 2011; Hartmeyer *et al.*, 2020).
649 Even the most conservative rock wall retreat rate ($71.2 \pm 2.8 \text{ mm a}^{-1}$) calculated for Grosse Grabe
650 (assuming the rockfall events of 2017-2020 are the only major activity since 1990 for the entire extent
651 of the monitored rock face (Figure 1)) is still very high compared to rock wall erosion rates of other
652 studies. Hartmeyer *et al.* (2020) reported very high retreat rates ($57.32 \pm 0.67 \text{ mm a}^{-1}$) for recently
653 deglaciaded areas along highly fractured weakness zones close to the glacial surface. Although the

654 monitored rock face in this study is not recently deglaciated, highly fractured lithology does play an
655 important role in the observed high rock wall retreat rates. In addition, and as discussed in the previous
656 section, we believe that the exposure of the base of the permafrost from the North side of the ridge
657 triggered progressive failure of the rock wall and is responsible for the unusually high erosion rates.
658 Although interpretation should be done with care, our results suggest that permafrost degradation in
659 these specific settings has the potential to alter the rock wall retreat rate drastically on a short time
660 scale. In the future, air temperatures are expected to increase in the European Alps (Gobiet *et al.*,
661 2014). Because of this, and the change in associated cryogenic and thermal stresses acting on rock
662 walls, Draebing, Krautblatter, and Hoffmann (2017) expect a shift from cryogenic driven rockfall on
663 north-exposed rock walls to thermally driven rockfall on south-facing rockwalls. If this occurs in narrow
664 ridge topography in areas experiencing marginal permafrost, exposure of deep bedrock permafrost
665 developed from the north side could lead to progressive failure of the rock wall, as observed in this
666 study. Although rock wall erosion rates are expected to decrease at the elevation of our study site due
667 to a shift of frost weathering to higher elevations (Draebing and Mayer 2021), they might first increase
668 due to scenario's similar to the one presented in this study. Moreover, the observed temporal
669 clustering of the rockfall events has an important implication for hazard management, potentially
670 endangering hikers making use of the hiking track in summer.

671 **5. Conclusion**

672 This research presents a detailed temporal and spatial record of the processes and events
673 before, during and after consecutive large rock- and cliff falls that occurred at a rock face at Grosse
674 Grabe in Mattertal (Western Swiss Alps) in 2019 and 2020. This rockfall record proved to be highly
675 valuable to gain insight in the preconditioning, preparatory and triggering factors involved, of use for
676 understanding similar rockfall happening elsewhere in the European Alps. We also show the potential
677 of combining multiple close-range remote sensing data for the detection of rockfall in high
678 mountain environments, where challenging field conditions do not allow in-situ measurements.
679 The integration of both high resolution topography datasets derived from TLS and UAV with seismic
680 observations resulted in a detailed overview of the exact timing and estimated volumes of all individual
681 rockfall events, as validated by the automatic camera.

682 The initial cause of the large consecutive rock- and cliff falls ($10^3 - 10^6 \text{ m}^3$) that occurred in the
683 summers of 2019 and 2020 are considered to be of geological nature with a pre-existing mesh of
684 discontinuities (mostly tectonic clefts and schistosity bedding). The south exposure makes this densely
685 fractured rock wall vulnerable for thermally induced failure mechanism on different timescales,
686 highlighted by the increased irreversible displacement observed in summer, the occurrence of rockfall
687 mostly in the second half of summer and in the (late) afternoon. The observed outward displacement

688 of the rock face prior to any rockfall suggest a toppling failure mechanism related to sub-vertical
689 fractures in the rock wall. A change in deformation geometry was observed 1.5 years before any
690 significant collapse, with an increase in the outward displacement at the top of the rock face. The
691 deformation was probably affecting frozen rock as well, indicating that permafrost degradation is a
692 potential preparatory factor. A large rockfall event at the end of August in 2019 exposed deep bedrock
693 permafrost, believed to be the base of the permafrost developed from the north side of the ridge,
694 triggering progressive failure of the rock wall due to thermal adjustment. This process quickly melted
695 the exposed and the subsurface ice and together with the unloading caused large rock- and cliff fall
696 events to occur in a short succession in the summer of 2019 and 2020. These events were often
697 preluded by precursory small-scale rockfall, believed to be triggered by active layer thickening, hours
698 before the larger volume detached. All rockfall activity ceased in the winter season when the process
699 of thermal adjustment is stalled due to colder temperatures. All site specific conditions, such as the
700 dense fracturation, the southerly aspect, the gentle dipping of the schistosity bedding and the large
701 cliff falls exposing deep bedrock permafrost, lead locally to very high rock wall erosion rates.

702 **DATA AVAILABILITY STATEMENT**

703 The datasets used and/or analysed during the current study are available from the corresponding
704 author on reasonable request.

705 **CONFLICT OF INTEREST**

706 The authors declare that there is no conflict of interest.

707

708 **References**

- 709 Abellán, A. *et al.* (2010) 'Detection and spatial prediction of rockfalls by means of terrestrial laser
710 scanner monitoring', *Geomorphology*. Elsevier, 119(3–4), pp. 162–171. doi:
711 10.1016/j.geomorph.2010.03.016.
- 712 Allen, S. and Huggel, C. (2013) 'Extremely warm temperatures as a potential cause of recent high
713 mountain rockfall', *Global and Planetary Change*, 107, pp. 59–69. doi:
714 10.1016/j.gloplacha.2013.04.007.
- 715 Baer, P. *et al.* (2017) 'Changing debris flow activity after sudden sediment input: a case study from the
716 Swiss Alps', *Geology Today*, 33(6), pp. 216–223. doi: 10.1111/gto.12211.
- 717 Bajni, G., Camera, C. and Apuani, T. (2020) 'Bajni, Greta, Corrado Camera, and Tiziana Apuani.
718 "Deciphering Rainfall and Freeze thaw cycles as long-term preparatory factors for alpine rockfalls', in
719 *EGU General Assembly Conference Abstracts.*, p. 6793.

720 Bakun-Mazor, D. *et al.* (2020) 'Thermally-Induced Wedging–Ratcheting Failure Mechanism in Rock
721 Slopes', *Rock Mechanics and Rock Engineering*, 53(6), pp. 2521–2538. doi: 10.1007/s00603-020-02075-
722 6.

723 Ballantyne, C. K. (2018) *Periglacial Geomorphology*. John Wiley & Sons.

724 Bearth, P. (1978) 'Geologischer Atlas der Schweiz 1:25 000, Karte 71. Blatt 1308. Swisstopo: St. Niklaus'.

725 Beniston, M. *et al.* (2018) 'The European mountain cryosphere: A review of its current state, trends,
726 and future challenges', *Cryosphere*, 12(2), pp. 759–794. doi: 10.5194/tc-12-759-2018.

727 Boeckli, L. *et al.* (2012) 'Permafrost distribution in the European Alps: Calculation and evaluation of an
728 index map and summary statistics', *Cryosphere*, 6(4), pp. 807–820. doi: 10.5194/tc-6-807-2012.

729 Collins, B. D. and Stock, G. M. (2016) 'Rockfall triggering by cyclic thermal stressing of exfoliation
730 fractures', *Nature Geoscience*. Nature Publishing Group, 9(5), pp. 395–400. doi: 10.1038/ngeo2686.

731 Cook, K. L. and Dietze, M. (2019) 'Short Communication: A simple workflow for robust low-cost UAV-
732 derived change detection without ground control points', *Earth Surface Dynamics Discussions*, 7(4),
733 pp. 1–15. doi: 10.5194/esurf-2019-27.

734 D'Amato, J. *et al.* (2016) 'Influence of meteorological factors on rockfall occurrence in a middle
735 mountain limestone cliff', *Natural Hazards and Earth System Sciences*, 16(3), pp. 719–735. doi:
736 10.5194/nhess-16-719-2016.

737 Dammeier, F. *et al.* (2011) 'Characterization of alpine rockslides using statistical analysis of seismic
738 signals', *Journal of Geophysical Research: Earth Surface*. Blackwell Publishing Ltd, 116(4). doi:
739 10.1029/2011JF002037.

740 Davies, M. C. R., Hamza, O. and Harris, C. (2001) 'The effect of rise in mean annual temperature on the
741 stability of rock slopes containing ice-filled discontinuities', *Permafrost and Periglacial Processes*. John
742 Wiley & Sons, Ltd., 12(1), pp. 137–144. doi: 10.1002/ppp.378.

743 Delaloye, R. *et al.* (2013) 'Rapidly moving rock glaciers in Mattertal', *Jahrestagung der Schweizerischen
744 Geomorphologischen Gesellschaft*, (i), pp. 21–31.

745 Delaloye, R. *et al.* (2014) *Blockgletscher und Hangrutschungen in Permafrostgebieten Departement für
746 Geowissenschaften, Blockgletscher und Hangrutschungen in Permafrostgebieten, Projekt 'Mattertal'
747 (2009-2013), Gemeinde St.-Niklaus und Randa, Abschlussbericht 2013. non publié, 121p.*

748 Delaloye, R. and Morard, S. (2011) 'Le glacier rocheux déstabilisé du Petit-Vélan (Val d'Entremont,
749 Valais): morphologie de surface, vitesses de déplacement et structure interne', in *La géomorphologie
750 alpine: entre patimoine et contrainte. Actes du colloque de la Société Suisse de Géomorphologie, 3-5
751 septembre 2009, Olivone (Géovisions n° 36). Institut de géographie, Université de Lausanne.*, pp. 197–
752 210.

753 Deparis, J. *et al.* (2008) 'Analysis of rock-fall and rock-fall avalanche seismograms in the French Alps',
754 *Bulletin of the Seismological Society of America*. GeoScienceWorld, pp. 1781–1796. doi:

755 10.1785/0120070082.

756 Dietze, M., Mohadjer, S., *et al.* (2017) 'Seismic monitoring of small alpine rockfalls-validity, precision
757 and limitations', *Earth Surface Dynamics*, 5(4), pp. 653–668. doi: 10.5194/esurf-5-653-2017.

758 Dietze, M., Turowski, J. M., *et al.* (2017) 'Spatiotemporal patterns, triggers and anatomies of seismically
759 detected rockfalls', *Earth Surface Dynamics*, 5(4), pp. 757–779. doi: 10.5194/esurf-5-757-2017.

760 Draebing, D. and Krautblatter, M. (2019) 'The Efficacy of Frost Weathering Processes in Alpine
761 Rockwalls', *Geophysical Research Letters*, 46(12), pp. 6516–6524. doi: 10.1029/2019GL081981.

762 Draebing, D., Krautblatter, M. and Dikau, R. (2014) 'Interaction of thermal and mechanical processes
763 in steep permafrost rock walls: A conceptual approach', *Geomorphology*. Elsevier, 226, pp. 226–235.
764 doi: 10.1016/j.geomorph.2014.08.009.

765 Draebing, D., Krautblatter, M. and Hoffmann, T. (2017) 'Thermo-cryogenic controls of fracture
766 kinematics in permafrost rockwalls', *Geophysical Research Letters*, 44(8), pp. 3535–3544. doi:
767 10.1002/2016GL072050.

768 Draebing, D. and Mayer, T. (2021) 'Topographic and Geologic Controls on Frost Cracking in Alpine
769 Rockwalls', *Journal of Geophysical Research: Earth Surface*. Blackwell Publishing Ltd, 126(6). doi:
770 10.1029/2021JF006163.

771 Dussauge, C., Grasso, J.-R. and Helmstetter, A. (2003) 'Statistical analysis of rockfall volume
772 distributions: Implications for rockfall dynamics', *Journal of Geophysical Research: Solid Earth*.
773 American Geophysical Union (AGU), 108(B6). doi: 10.1029/2001jb000650.

774 Eissler, H. K. and Kanamori, H. (1987) 'A single-force model for the 1975 Kalapana, Hawaii, Earthquake',
775 *Journal of Geophysical Research*. American Geophysical Union (AGU), 92(B6), p. 4827. doi:
776 10.1029/jb092ib06p04827.

777 Fischer, L. *et al.* (2011) 'Monitoring topographic changes in a periglacial high-mountain face using high-
778 resolution DTMs, Monte Rosa East Face, Italian Alps', *Permafrost and Periglacial Processes*. John Wiley
779 & Sons, Ltd, 22(2), pp. 140–152. doi: 10.1002/ppp.717.

780 Fischer, L. *et al.* (2012) 'On the influence of topographic, geological and cryospheric factors on rock
781 avalanches and rockfalls in high-mountain areas', *Natural Hazards and Earth System Science*, 12(1), pp.
782 241–254. doi: 10.5194/nhess-12-241-2012.

783 Fischer, L. *et al.* (2012) 'On the influence of topographic, geological and cryospheric factors on rock
784 avalanches and rockfalls in high-mountain areas', *Natural Hazards and Earth System Science*, 12(1), pp.
785 241–254. doi: 10.5194/nhess-12-241-2012.

786 Fischer, M. *et al.* (2016) 'Application and validation of long-range terrestrial laser scanning to monitor
787 the mass balance of very small glaciers in the Swiss Alps', *Cryosphere*, 10(3), pp. 1279–1295. doi:
788 10.5194/tc-10-1279-2016.

789 Gardner, J. S. (1983) 'Rockfall frequency and distribution in the Highwood Pass area, Canadian Rocky

790 Mountains', *Zeitschrift für Geomorphologie*, 27(3), pp. 311–324. doi: 10.1127/zfg/27/1983/311.

791 Gischig, V. *et al.* (2009) 'Identification of active release planes using ground-based differential InSAR at
792 the Randa rock slope instability, Switzerland', *Natural Hazards and Earth System Science*. Copernicus
793 GmbH, 9(6), pp. 2027–2038. doi: 10.5194/nhess-9-2027-2009.

794 Gischig, V. S. *et al.* (2011) 'Thermomechanical forcing of deep rock slope deformation: 1. Conceptual
795 study of a simplified slope', *Journal of Geophysical Research: Earth Surface*, 116(4), p. F04010. doi:
796 10.1029/2011JF002006.

797 Gobiet, A. *et al.* (2014) '21st century climate change in the European Alps-A review', *Science of the
798 Total Environment*, 493, pp. 1138–1151. doi: 10.1016/j.scitotenv.2013.07.050.

799 Goodman, R. E. and Kieffer, D. S. (2000) 'Behavior of Rock in Slopes', *Journal of Geotechnical and
800 Geoenvironmental Engineering*. American Society of Civil Engineers (ASCE), 126(8), pp. 675–684. doi:
801 10.1061/(asce)1090-0241(2000)126:8(675).

802 Gruber, S. (2004) 'Permafrost thaw and destabilization of Alpine rock walls in the hot summer of 2003',
803 *Geophysical Research Letters*, 31(13), p. L13504. doi: 10.1029/2004GL020051.

804 Gruber, S. and Haeberli, W. (2007) 'Permafrost in steep bedrock slopes and its temperatures-related
805 destabilization following climate change', *Journal of Geophysical Research: Earth Surface*, 112(2), pp.
806 1–10. doi: 10.1029/2006JF000547.

807 Guillemot, A. *et al.* (2020) 'Seismic monitoring in the Gugla rock glacier (Switzerland): ambient noise
808 correlation, microseismicity and modelling', *Geophysical Journal International*. Oxford University Press
809 (OUP), 221(3), pp. 1719–1735. doi: 10.1093/gji/ggaa097.

810 Gunzburger, Y., Merrien-Soukatchoff, V. and Guglielmi, Y. (2005) 'Influence of daily surface
811 temperature fluctuations on rock slope stability: Case study of the Rochers de Valabres slope (France)',
812 *International Journal of Rock Mechanics and Mining Sciences*. Pergamon, 42(3), pp. 331–349. doi:
813 10.1016/j.ijrmms.2004.11.003.

814 Haeberli, W. and Beniston, M. (1998) 'Climate change and its impacts on glaciers and permafrost in
815 the Alps', *Ambio*, 27, pp. 258–265.

816 Hartmeyer, I. *et al.* (2020) 'A 6-year lidar survey reveals enhanced rockwall retreat and modified
817 rockfall magnitudes/frequencies in deglaciating cirques', *Earth Surface Dynamics*. Copernicus GmbH,
818 8(3), pp. 753–768. doi: 10.5194/esurf-8-753-2020.

819 Hasler, A. *et al.* (2011) 'Advective heat transport in frozen rock clefts: Conceptual model, laboratory
820 experiments and numerical simulation', *Permafrost and Periglacial Processes*. John Wiley & Sons, Ltd,
821 22(4), pp. 378–389. doi: 10.1002/ppp.737.

822 Hasler, A., Gruber, S. and Beutel, J. (2012) 'Kinematics of steep bedrock permafrost', *Journal of
823 Geophysical Research: Earth Surface*. John Wiley & Sons, Ltd, 117(1), p. n/a-n/a. doi:
824 10.1029/2011JF001981.

825 Hasler, A., Gruber, S. and Haeberli, W. (2011) 'Temperature variability and offset in steep alpine rock
826 and ice faces', *Cryosphere*, 5(4), pp. 977–988. doi: 10.5194/tc-5-977-2011.

827 Helmstetter, A. and Garambois, S. (2010) 'Seismic monitoring of Schilienne rockslide (French Alps):
828 Analysis of seismic signals and their correlation with rainfalls', *Journal of Geophysical Research: Earth
829 Surface*, 115(3), pp. 1–15. doi: 10.1029/2009JF001532.

830 Hendrickx, H. *et al.* (2020) 'Talus slope geomorphology investigated at multiple time scales from high-
831 resolution topographic surveys and historical aerial photographs (Sanetsch Pass, Switzerland)', *Earth
832 Surface Processes and Landforms*, p. esp.4989. doi: 10.1002/esp.4989.

833 Huggel, C. *et al.* (2012) 'Ice thawing, mountains falling-are alpine rock slope failures increasing',
834 *Geology Today*. John Wiley & Sons, Ltd, 28(3), pp. 98–104. doi: 10.1111/j.1365-2451.2012.00836.x.

835 Kanamori, H. and Anderson, D. L. (1975) 'Theoretical basis of some empirical relations in seismology',
836 *Bulletin of the Seismological Society of America*, 65(5), pp. 1073–1095.

837 Kanamori, H. and Given, J. W. (1982) 'Analysis of long-period seismic waves excited by the May 18,
838 1980, eruption of Mount St Helens - a terrestrial monopole?', *Journal of Geophysical Research*. John
839 Wiley & Sons, Ltd, 87(B7), pp. 5422–5432. doi: 10.1029/JB087iB07p05422.

840 Keefer, K. D. (1984) 'Landslides caused by earthquakes', *GSA Bulletin*, 95(4), pp. 406–421. doi:
841 [https://doi.org/10.1130/0016-7606\(1984\)95&l;lt;406:LCBE&l;gt;2.0.CO;2](https://doi.org/10.1130/0016-7606(1984)95&l;lt;406:LCBE&l;gt;2.0.CO;2).

842 Kenner, R. *et al.* (2011) 'Investigation of rock and ice loss in a recently deglaciated mountain rock wall
843 using terrestrial laser scanning: Gemsstock, Swiss Alps', *Cold Regions Science and Technology*. Elsevier,
844 67(3), pp. 157–164. doi: 10.1016/j.coldregions.2011.04.006.

845 Kenner, R., Noetzli, J., *et al.* (2019) 'Distinguishing ice-rich and ice-poor permafrost to map ground
846 temperatures and ground ice occurrence in the Swiss Alps', *Cryosphere*, 13(7), pp. 1925–1941. doi:
847 10.5194/tc-13-1925-2019.

848 Kenner, R., Bühler, Y., *et al.* (2019) *Ereignisanalyse. Felssturz und Lwne vom 19.3.2019 am Flüela
849 Wisshorn (Davos, Graubünden)*.

850 Krautblatter, M. and Dikau, R. (2007) 'Towards a uniform concept for the comparison and extrapolation
851 of rockwall retreat and rockfall supply', *Geografiska Annaler, Series A: Physical Geography*. Blackwell
852 Publishing Ltd, 89(1), pp. 21–40. doi: 10.1111/j.1468-0459.2007.00305.x.

853 Krautblatter, M., Funk, D. and Günzel, F. K. (2013) 'Why permafrost rocks become unstable: A rock-ice-
854 mechanical model in time and space', *Earth Surface Processes and Landforms*, 38(8), pp. 876–887. doi:
855 10.1002/esp.3374.

856 Krautblatter, M. and Moore, J. R. (2014) 'Rock slope instability and erosion: Toward improved process
857 understanding', *Earth Surface Processes and Landforms*. John Wiley & Sons, Ltd, pp. 1273–1278. doi:
858 10.1002/esp.3578.

859 Kummert, M. and Delaloye, R. (2018) 'Mapping and quantifying sediment transfer between the front

860 of rapidly moving rock glaciers and torrential gullies', *Geomorphology*. Elsevier, 309, pp. 60–76. doi:
861 10.1016/j.geomorph.2018.02.021.

862 Kummert, M., Delaloye, R. and Braillard, L. (2018) 'Erosion and sediment transfer processes at the front
863 of rapidly moving rock glaciers: Systematic observations with automatic cameras in the western Swiss
864 Alps', *Permafrost and Periglacial Processes*, 29(1), pp. 21–33. doi: 10.1002/ppp.1960.

865 Lague, D., Brodu, N. and Leroux, J. (2013) 'Accurate 3D comparison of complex topography with
866 terrestrial laser scanner: Application to the Rangitikei canyon (N-Z)', *ISPRS Journal of Photogrammetry
867 and Remote Sensing*. International Society for Photogrammetry and Remote Sensing, Inc. (ISPRS), 82,
868 pp. 10–26. doi: 10.1016/j.isprsjprs.2013.04.009.

869 Leinauer, J., Jacobs, B. and Krautblatter, M. (2020) 'Process dynamics , real time monitoring and early
870 warning at an imminent cliff fall (Hochvogel , Allgäu Alps)', in *EGU General Assembly 2020*. Online, pp.
871 EGU2020-19073.

872 Leith, K. *et al.* (2014) 'Subglacial extensional fracture development and implications for Alpine Valley
873 evolution', *Journal of Geophysical Research: Earth Surface*. John Wiley & Sons, Ltd, 119(1), pp. 62–81.
874 doi: 10.1002/2012JF002691.

875 Luckman, B. H. (2013) 'Processes , Transport , Deposition , and Landforms : Rockfall', in Shroder, J. F.
876 (ed.) *Treatise on Geomorphology*. 7th edn. San Diego: Academic Press, pp. 174–182. doi:
877 10.1016/B978-0-12-374739-6.00162-7.

878 Magnin, F. *et al.* (2017) 'Modelling rock wall permafrost degradation in the Mont Blanc massif from
879 the LIA to the end of the 21st century', *Cryosphere*. Copernicus GmbH, 11(4), pp. 1813–1834. doi:
880 10.5194/tc-11-1813-2017.

881 Mamot, P. *et al.* (2018) 'A temperature-and stress-controlled failure criterion for ice-filled permafrost
882 rock joints', *Cryosphere*. Copernicus GmbH, 12(10), pp. 3333–3353. doi: 10.5194/tc-12-3333-2018.

883 Matsuoka, N. (2008) 'Frost weathering and rockwall erosion in the southeastern Swiss Alps: Long-term
884 (1994–2006) observations', *Geomorphology*. Elsevier, 99(1–4), pp. 353–368. doi:
885 10.1016/j.geomorph.2007.11.013.

886 Matsuoka, N. (2019) 'A multi-method monitoring of timing, magnitude and origin of rockfall activity in
887 the Japanese Alps', *Geomorphology*. Elsevier, 336, pp. 65–76. doi: 10.1016/j.geomorph.2019.03.023.

888 McColl, S. T. and Draebing, D. (2019) 'Rock Slope Instability in the Proglacial Zone: State of the Art', in.
889 Springer, Cham, pp. 119–141. doi: 10.1007/978-3-319-94184-4_8.

890 Moore, J. R. *et al.* (2011) 'Air circulation in deep fractures and the temperature field of an alpine rock
891 slope', *Earth Surface Processes and Landforms*. John Wiley & Sons, Ltd, 36(15), pp. 1985–1996. doi:
892 10.1002/esp.2217.

893 Nishii, R. and Matsuoka, N. (2012) 'Kinematics of an alpine retrogressive rockslide in the Japanese Alps',
894 *Earth Surface Processes and Landforms*. John Wiley & Sons, Ltd, 37(15), pp. 1641–1650. doi:

895 10.1002/esp.3298.

896 Noetzli, J. *et al.* (2007) 'Three-dimensional distribution and evolution of permafrost temperatures in
897 idealized high-mountain topography', *Journal of Geophysical Research: Earth Surface*, 112(2), p.
898 F02S13. doi: 10.1029/2006JF000545.

899 PERMOS (2016) *Permafrost in Switzerland 2010/2011 to 2013/2014*. Edited by J. Noetzli, R. Luethi, and
900 B. Staub. Glaciological Report (Permafrost) No. 12-15 of the Cryospheric Commission of the Swiss
901 Academy of Sciences.

902 Phillips, M. *et al.* (2016) 'Seasonally intermittent water flow through deep fractures in an Alpine Rock
903 Ridge: Gemsstock, Central Swiss Alps', *Cold Regions Science and Technology*. Elsevier, 125, pp. 117–
904 127. doi: 10.1016/j.coldregions.2016.02.010.

905 Phillips, M. *et al.* (2017) 'Rock slope failure in a recently deglaciated permafrost rock wall at Piz Kesch
906 (Eastern Swiss Alps), February 2014', *Earth Surface Processes and Landforms*. John Wiley and Sons Ltd,
907 42(3), pp. 426–438. doi: 10.1002/esp.3992.

908 Ravanel, L., Magnin, F. and Deline, P. (2017) 'Impacts of the 2003 and 2015 summer heatwaves on
909 permafrost-affected rock-walls in the Mont Blanc massif', *Science of the Total Environment*. Elsevier
910 B.V., 609, pp. 132–143. doi: 10.1016/j.scitotenv.2017.07.055.

911 Le Roy, G. *et al.* (2019) 'Seismic Analysis of the Detachment and Impact Phases of a Rockfall and
912 Application for Estimating Rockfall Volume and Free-Fall Height', *Journal of Geophysical Research:
913 Earth Surface*, 124(11), pp. 2602–2622. doi: 10.1029/2019JF004999.

914 Sala, Z., Hutchinson, D. J. and Harrap, R. (2019) 'Simulation of fragmental rockfalls detected using
915 terrestrial laser scans from rock slopes in south-central British Columbia, Canada', *Natural Hazards and
916 Earth System Sciences*, 19(11), pp. 2385–2404. doi: 10.5194/nhess-19-2385-2019.

917 Sanders, J. W. *et al.* (2013) 'The sediment budget of an Alpine cirque', *Bulletin of the Geological Society
918 of America*. GeoScienceWorld, 125(1–2), pp. 229–248. doi: 10.1130/B30688.1.

919 Sass (2005a) 'Rock moisture measurements: Techniques, results, and implications for weathering',
920 *Earth Surface Processes and Landforms*. John Wiley & Sons, Ltd, 30(3), pp. 359–374. doi:
921 10.1002/esp.1214.

922 Sass (2005b) 'Spatial patterns of rockfall intensity in the northern Alps', *Zeitschrift für Geomorphologie*,
923 138, pp. 51–65.

924 Sass (2005c) 'Temporal variability of rockfall in the Bavarian Alps, Germany', *Arctic, Antarctic, and
925 Alpine Research*, 37(4), pp. 564–573. doi: 10.1657/1523-0430(2005)037[0564:TVORIT]2.0.CO;2.

926 Sass, O. and Wollny, K. (2001) 'Investigations regarding alpine talus slopes using ground-penetrating
927 radar (GPR) in the Bavarian Alps, Germany', *Earth Surface Processes and Landforms*. John Wiley & Sons,
928 Ltd, 26(10), pp. 1071–1086. doi: 10.1002/esp.254.

929 *ShapeMetric3D* (2021). Available at: <https://3gsm.at/produkte/shape-metrix/> (Accessed: 19 October

930 2021).

931 Stock, G. M. *et al.* (2012) 'Progressive failure of sheeted rock slopes: the 2009–2010 Rhombus Wall
932 rock falls in Yosemite Valley, California, USA', *Earth Surface Processes and Landforms*. John Wiley &
933 Sons, Ltd, 37(5), pp. 546–561. doi: 10.1002/ESP.3192.

934 Stoffel, M. and Huggel, C. (2012) 'Effects of climate change on mass movements in mountain
935 environments', *Progress in Physical Geography*. SAGE Publications, 36(3), pp. 421–439. doi:
936 10.1177/0309133312441010.

937 Stoffel, M., Tiranti, D. and Huggel, C. (2014) 'Climate change impacts on mass movements - Case
938 studies from the European Alps', *Science of the Total Environment*, 493, pp. 1255–1266. doi:
939 10.1016/j.scitotenv.2014.02.102.

940 *Study sites - Grosse Grabe* (2021). Available at:
941 <https://www3.unifr.ch/geo/geomorphology/en/resources/study-sites/grosse-grabe.html> (Accessed:
942 3 May 2021).

943 *UZH - The PermaSense Consortium* (2021). Available at: <https://www.permasense.ch/en.html>
944 (Accessed: 28 September 2021).

945 Vilajosana, I. *et al.* (2008) 'Rockfall induced seismic signals: Case study in Montserrat, Catalonia',
946 *Natural Hazards and Earth System Science*. European Geosciences Union, 8(4), pp. 805–812. doi:
947 10.5194/nhess-8-805-2008.

948 Walter, F. *et al.* (2019) 'Direct observations of a three million cubic meter rock-slope collapse with
949 almost immediate initiation of ensuing debris flows', *Geomorphology*, p. 106933. doi:
950 10.1016/j.geomorph.2019.106933.

951 Weber, S. *et al.* (2017) 'Quantifying irreversible movement in steep, fractured bedrock permafrost on
952 Matterhorn (CH)', *Cryosphere*, 11(1), pp. 567–583. doi: 10.5194/tc-11-567-2017.

953